Experimental Investigation of Relative Permeability Upscaling from the Micro-Scale to the Macro-Scale

Semi-Annual Progress Report

Reporting Period Start Date: March 1, 2001
Reporting Period End Date: Jul 31, 2001

JiangTao Cheng, Ping Yu, William Headley, Nicholas Giordao, Mirela Mustata , Daiquan Chen, Nathan Cooper, David D. Nolte and Laura J. Pyrak-Nolte

December 2001

DOE Award: DE-AC26-99BC15207

Purdue Research Foundation
Department of Physics
1396 Physics Building, Room 166
West Lafayette, Indiana 47907-1396

Abstract: The principal challenge of upscaling techniques for multi-phase fluid dynamics in porous media is to determine which properties on the micro-scale can be used to predict macroscopic flow and spatial distribution of phases at core- and field-scales. The most notable outcome of recent theories is the identification of interfacial areas per volume for multiple phases as a fundamental parameter that determines much of the multi-phase properties of the porous medium. A formal program of experimental research was begun to directly test upscaling theories in fluid flow through porous media by comparing measurements of relative permeability and capillary-saturation with measurements of interfacial area per volume. During this reporting period, we have shown experimentally and theoretically that the optical coherence imaging system is optimized for sandstone. The measurement of interfacial area per volume (IAV), capillary pressure and saturation in two dimensional micro-models structures that are statistically similar to real porous media has shown the existence of a unique relationship among these hydraulic parameters. The measurement of interfacial area per volume on a three-dimensional natural sample, i.e., sandstone, has the same length-scale as the values of IAV determined for the two-dimensional micro-models.

Table of Contents

List of Figures

List of Tables

Executive Summary

Direct experimental tests of upscaling theories in fluid flow through porous media will be made by comparing measurements of relative permeability and capillary-saturation with measurements of interfacial area per volume. These experiments are performed from the pore-scale (microns) to the core-scale (centimeters), spanning four orders of magnitude in size. Three experimental objectives provide the data for rigorous tests of upscaling theories. First, holographic laser imaging techniques will acquire pore-scale three-dimensional optical images of the pore geometry in reservoir sandstones. This technique uses unique properties of coherent light to see through drilling muds and into the sandstone. Second, laboratory micro-models with matched topological properties based on the data from the pore imaging will make it possible to measure interfacial area per volume in scientifically controlled imbibition and drainage experiments, combined with measurements of capillary-pressure-saturation data and relative permeability. Third, core-scale experiments of relative permeability and capillary-saturation, and metal casts of the pore geometry, will be compared with the pore-scale data of the first two objectives. The data from all these objectives will provide the first complete picture over such a large dynamic range. It will make it possible to answer the principal question concerning flow upscaling: which microscopic measurements are most useful for predicting macroscopic flow properties of an oil reservoir. The tangible outcome of this work will be explicit data connecting interfacial areas, or other relevant geometric micro-scale data, with macroscopic hydraulic properties. In addition, we show strong industrial interest in testing and commercializing the unique down-hole laser imaging technology that can be transferred to the oil-industry service-company sector.

During this reporting period, we have shown experimentally and theoretically that the optical coherence imaging system is optimized for sandstone. The measurement of interfacial area per volume (IAV), capillary pressure and saturation in two dimensional micro-models structures that are statistically similar to real porous media has shown the existence of a unique relationship among these hydraulic parameters. The measurement of interfacial area per volume on a three-dimensional natural sample, i.e., sandstone, has determined that the length-scales (~100 microns) are the same for the values of IAV determined from the micro-models and the sandstone.

1.0 Introduction

1.1 Summary of Project Description

Standard expressions of multi-phase flow in porous media based on modifications of Darcy's Law (Darcy, 1856) have crippling deficiencies that make them undesirable to use for critical operations such as tertiary recovery of oil from depleted reservoirs. The primary difficulty in these empirical expressions are their violation of rigorous conservation laws. New theories based on rigorous volume averaging theorems and fundamental thermodynamic principles of phase boundaries have emerged in the past decade to replace the old empirical rules (Hassanizadeh and Gray, 1979; Gray, 1983; Kalaydjian, 1990). The most notable outcome of these theories is the identification of interfacial areas per volume for multiple phases as fundamental parameters that determine much of the multi-phase properties of the porous medium (Muccino, Gray and Ferrand, 1998).

Interfacial areas per volume provide natural descriptions of fundamental physical processes in porous media. For instance, thermodynamic energies are proportional to interfacial areas, and interfacial areas per volume represent a form of energy density. Gradients in energy densities define the dynamical pressures that drive the movement and distribution of phases within a complex topology. Interfacial areas per volume in a porous medium therefore represent a three-dimensional potential energy landscape.

Interfacial areas per volume also provide a natural yard-stick for defining the role of scale in multiphase fluid properties. The dimensional units of interfacial area per volume is a spatial frequency (inverse length) that breaks scale invariance. A useful illustration (Gray, 1998) of this scale-defining role can be made by considering an image of a pore-geometry containing only a single phase. Without a measurement scale, it is impossible to state what the physical size of the system is. However, when two phases such as water and air are both present, the length scale becomes obvious. At small scales, the water-air interface is drawn into the pore throats, while at large scales the water puddles in the large void volumes.

Therefore, the interfacial areas between phases define a length scale. Whenever a physical system has an intrinsic length scale, the physics of the system can be divided into two regimes: one where sample sizes are larger than the intrinsic length scale, and the other where information is obtained on scales smaller than the intrinsic length scale. Breaking scale invariance makes it possible to define representative elementary volumes (REV) and to apply averaging theorems. Combining the averaging theorems with thermodynamics further constrains the possible types of constitutive equations that can rigorously describe multiphase fluid properties in porous media.

As a consequence of this theoretical framework, interfacial areas per volume (IAV) take on a more important role than simple volume saturation . This important role of IAV is clear because a single value of relative volume saturation can correspond to infinitely different distributions of two phases within the volume. Large values of IAV relate to a finely distributed phase that can block pore throats and seriously affect permeability, while small values of IAV relate to gross separations of phases, with large connected volumes of the phase that can flow unimpeded through the network. Significant numerical studies have been performed on the relationships between capillary-saturation and interfacial area. Reeves and Celia (1995) developed a numerical model that scans over repetitive imbibition and drainage while tracking the interfacial area for each loop. These studies pointed to a non-unique relationship between interfacial area and partial saturation, although a family of curves did emerge that lies within a localized part of the parameter space defined by area and saturation.

The numerical studies illustrate the importance of continued and extensive experimental studies and tests of upscaling theories, and in particular tests of the role of interfacial area per volume in determining macroscopic flow properties. While oil recovery predictions should certainly include IAV as critical parameters, it is important to test whether other microscopic parameters also contribute to the macroscopic behavior. For instance, scale invariance of interfacial areas, even over restricted length scales, could present serious challenges to the averaging theorems, and could modify the presumed role of interfacial area in determining

macroscopic flow properties. The principal objective of our proposed upscaling approach is to experimentally measure many microscopic geometric parameters of the flow system over many scales, and connect these microscopic measurements with macroscopic flow behavior.

1.2 Project Objectives

The proposed work for this contract has three objectives that will provide rigorous experimental tests of upscaling theories. The objectives are:

1) To use holographic laser imaging techniques to acquire pore-scale three-dimensional optical images of the pore geometry in reservoir sandstones. This technique uses unique properties of coherent light to see through drilling muds and up to a millimeter into the sandstone. This data forms the basis of upscaling experiments to test theories of interfacial area per volume.

2) To construct laboratory micro-models with matched topological properties based on the data from the pore imaging. Interfacial area per volume will be measured directly in controlled imbibition and drainage experiments, together with capillary-pressure-saturation data and relative permeability data. This set of interrelated data will allow rigorous testing of upscaling theories.

3) To perform core-scale experiments of relative permeability and capillary-saturation, and to make metal casts of the pore geometry and interfacial area per volume. This core-scale data (including pore-scale from the metal casts) will be compared with the pore-scale data of the first two objectives, extending the observation scales over four orders of magnitude.

2.0 Experimental

2.1 Optical Coherence Imaging

2.1.1 Sample Preparation

The demand for high optical quality Multiple Quantum Well (MQW) devices has prompted an overhaul in the previous methods of their fabrication. The following summary highlights these changes by examining each of the six major steps in fabrication: dicing, device/glass slide bonding, mechanical lapping, chemical etching, flashing, and contacting. More information may be obtained regarding the processing of these devices from ref 1.

2.1.1.1 Dicing

The quantum wells used are grown, via Molecular Beam Epitaxy (MBE), by either Dr. M. R. Melloch of the Electrical Engineering Department at Purdue University, or an external company QED, Inc. The growth is deposited on undoped GaAs 3" wafers. The wafer is then diced up into small pieces, typically 2mm by 7 mm. The actual size depends on the desired optical area of the device.

Some small, subtle changes were made in hopes to reduce possible damage to the devices during the substrate-to-glass-side bonding. First, the cleaved material is blown off with canned air to prevent scratches caused by the debris of previous cuts. They are then rinsed with methanol to remove any debris that is electrostatically bonded to the surface. A second method was attempted to attempt to reduce chipping around the device during dicing as seen in Figure 1. The substrate was flipped over so that the device area was facing down so that the cuts were made to the substrate side of the wafer. Upon trying this method with several devices it was determined that this actually made the chipping worse so this method was abandoned.

2.1.1.2 Device/Glass Slide Bonding

After the wafer has been diced into usable portions, the substrate is attached to a one-millimeter thick glass slide that has been cut into a one-inch by ~ 1/2 inch piece. The side of

the substrate with the MBE grown quantum wells (called the device) is glued to the slide using an optical epoxy.

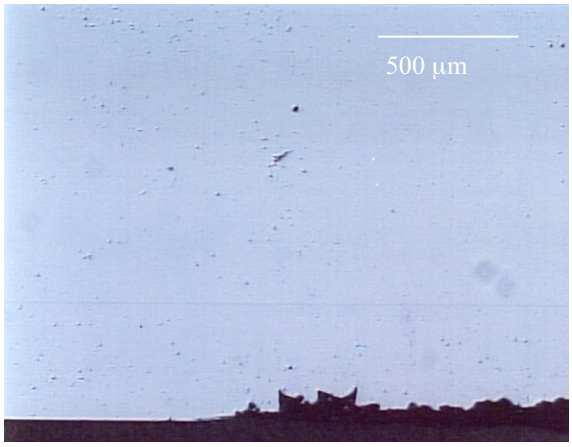

Figure 1. Debris on the material causing damage to the device. Chipping is also seen along the bottom edge of the picture.

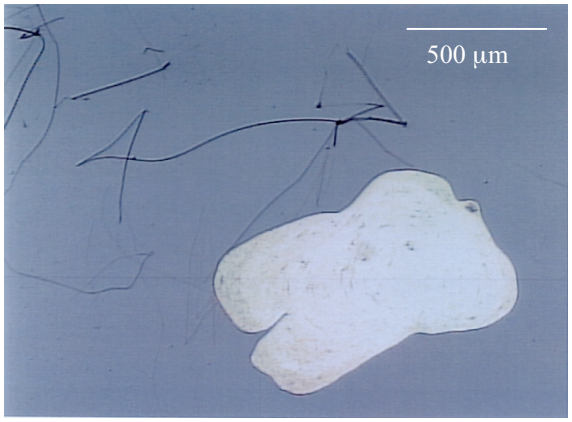

Figure 2. A worst-case example of bubbles and scratches on a device.

The epoxy used currently is a two-part optical epoxy. It was noticed that, upon mixing the epoxy, small bubbles could become trapped within the mixture. An example of a trapped bubble is shown in Figure 2. This creates two serious problems. One is that the bubbles, due to the index mismatch of the epoxy (n=1.54) with air, causes a scattering center. The other is that when fabrication is completed, these bubbles may be pushing out on the one-micron thick device causing the device to flake off in that region. We came up with a two-part solution to this problem.

First, the epoxy was heated in an 85°C oven for approximately five minutes. The heating reduces its viscosity so that upon mixing with the hardener trapped bubbles are able to float to the surface and ultimately free from the mixture. Then the mixed epoxy was placed in a desiccator (Figure 3) for several minutes in an attempt to outgas any remaining bubbles. This solution has worked because neither trapped bubbles have been observed nor has any flaking of devices been seen since its inception.

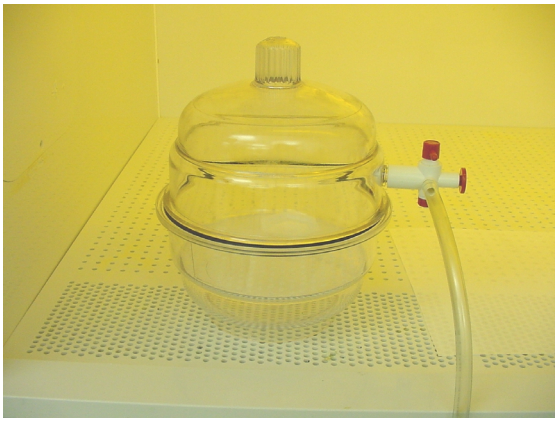

Figure 3. Desiccator used to remove bubbles from the epoxy.

Even though improvements have been made to the usage of the epoxy above, several one part epoxies are currently being investigated. They are made by Norland (part number 83H and 61) and distributed by Edmund Scientific. Being a one-part epoxy, no mixing is required, and it is therefore less prone to problems with bubbles. Also, its curing time is ten minutes in a 125°C oven for the 83H type versus 1.5 hours in an 85°C oven for the two-part epoxy. The 61-type epoxy is cured using an ultraviolet lamp with an exposure time of 10 minutes. Thus far, these epoxies have met with mixed results. They both adhere well to the glass slides and perform well under lapping and chemical etching. However, 50% of the devices made with the 83H-type epoxy have exhibited delaminating of the device from the slide shown in Figures 4 and 5. It is unclear as to why the devices are delaminating and so the use of this epoxy has been put on hold until the reason can be determined. The 61-type epoxy has been recently acquired and testing will begin soon.

Another improvement was made to the bonding step of fabrication. Previously, the epoxy was placed on the glass slide and then the substrate was pressed onto the slide with tweezers. A rotating motion was done to displace as much epoxy as possible between the slide and substrate. Also, the motion seemed to help remove any bubbles that may have become trapped. The problem with the rotating motion was that any type of debris on the order of a micron that may have made its way into the epoxy would scratch the surface and ruin the optical quality of the device. The current method is to initially place the device at an angle in the epoxy and then push down without using a rotating motion as shown in

Figure 6. As the device is pushed down, the epoxy escapes from one end. This method has met with good results. No scratches or bubbles have been seen since this method was introduced.

Finally, high optical quality pieces of plastic are being investigated to replace the glass slides. The plastic is a 2"x2" "window" sold by Edmund Scientific and is cut into 1/2"x 1" pieces. It is resistant to all chemicals used in the processing of these devices, especially HF. Therefore the methods to protect the glass from the HF are no longer needed. The results of its use thus far have been poor. Two devices were made with the plastic as a substrate. Both devices shattered when after the HF flash was completed. It is felt that the strain between the epoxy/device/plastic was too large, thereby cracking the devices when they reached their final thickness of only several microns. This strain may be reduced or eliminated by the use of a one-part epoxy. The devices discussed above were made with the two-part epoxy. Therefore they were subjected to a temperature of 85°C for 1.5 hours to cure the epoxy. It is felt that the mismatch in the thermal coefficients of expansions for the various materials created a strain that eventually caused the device to crack. Therefore the use of plastic as a replacement for the glass slides is still under investigation.

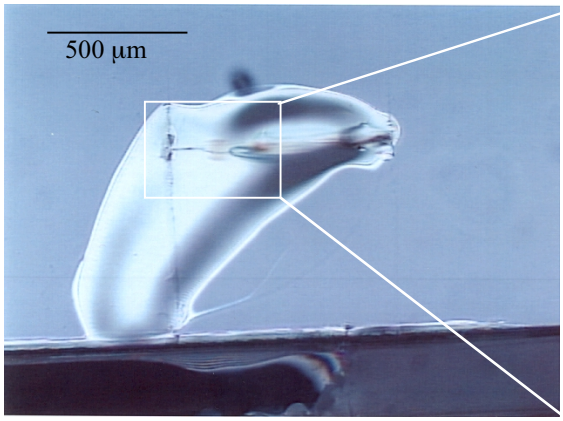

Figure 4. Device delamination viewed through the slide.

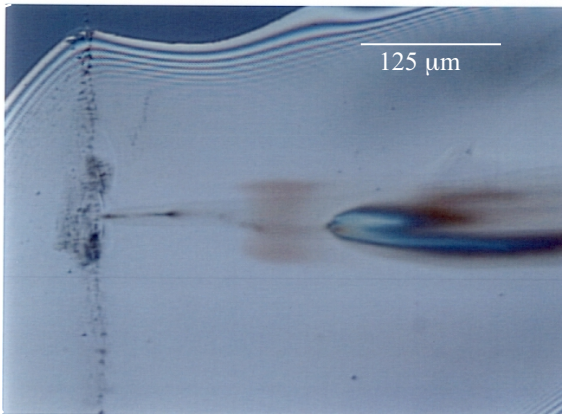

Figure 5. Close-up of Figure 3.

2.1.1.3 Lapping

After the epoxy is allowed to cure, the devices are lapped to remove all but the last one hundred microns or so of the substrate. Several key changes have been made in this step. The first is the attachment of the device to the lapper. Previously, materials such as black

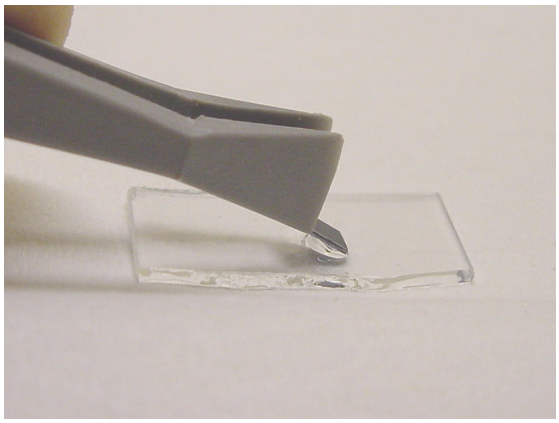

Figure 6. Device angled to the epoxy.

wax were used to make the attachment. However to attach and remove the device it was necessary to heat it. For attachment purposes this poses no problem, but for removal purposes this could be. At less than one hundred microns thick the device may become susceptible to cracking during heating. The new method for attachment is to use double-sided transparent tape. The tape does an excellent job of holding the device to the lapper during lapping. Also, by holding the lapper under running water while gently prying, the device comes off easily. This method has solved several problems seen in the past such as scratches to the glass caused by the wax.

A second method has recently been implemented due to problems seen in the following step of fabrication. The chemical etch would become anisotropic especially near the edges of the device. This problem is discussed in the next section. It was found that if the devices were lapped down to a thickness of ~70 microns instead of the previous limit of 100-130 microns that the anisotropy of the etch was greatly reduced or eliminated altogether. There is a problem of lapping too far in that as the device gets thinner, the greater the risk of

strain-induced cracking. However no evidence of cracking has been seen on devices that have been lapped to the new thickness.

2.1.1.4 Chemical Etch

Once the devices have reached the desired thickness, they are then subjected to a chemical etch to remove the remaining substrate. This is the most critical step of fabrication. Many if not all device fabrication failures originate in this step. One major problem occurs in this step: substrate is being left along the edges of the device. Several microscope images are shown in figure 7. If this remaining substrate spans the two contacts a short is incurred which may destroy the device once a field is applied. Attempts at allowing the device to stay in the etch longer to remove all of the substrate once the AlGaAs stop-etch layer has been reached have not been successful. The stop-etch layer only slows the etch and is not thick enough to sustain prolonged periods in the etch. The result is the overetching of the device into the quantum well layer. It is felt that the anisotropy of the etch near the edges is due to the lip created by the epoxy as the device is etched. By lapping the device more, less of a lip is left as the device etches. Also, since there is a lifetime of 30-45 minutes on the etch, a thinner device etches quicker and therefore takes advantage of the isotropy of the etch.

Another method has been implemented in conjunction with the extra thinning of the devices. A magnetic stirring bar has been added to the etch to increase the etchant movement over the devices, especially along the edges. It is unclear at this time as to the effect the stirring rod has on the etching quality due to slight variations in mixtures as well as the integrity of the chemicals themselves for each batch of etchant.

One final method recently introduced is the use of a cotton swab to brush the devices as they initially begin to etch as shown in figure 8. It has been noted that some of the device begin to form a coating that blocks the etchant. This coating seems to be more prevalent near the edges of the devices and is believed to be the cause of the remaining substrate near the edges as discussed above. The brushing is only done for the first few minutes that they are in the etchant. It is believed that further brushing may crack the device as it becomes thinner. The results of method have been excellent. The problems discussed above with the remaining substrate have been eliminated.

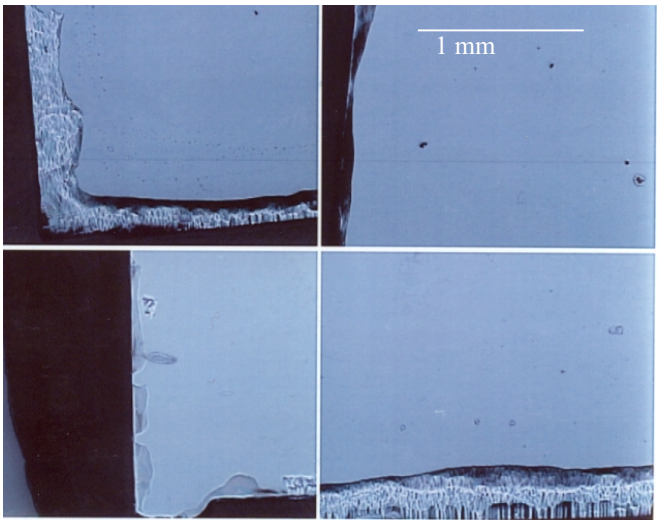

Figure 7. Various images of substrate residue near the edges.

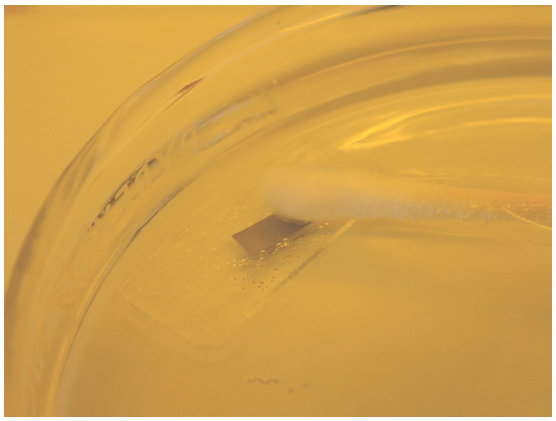

Figure 8. Device swabbed to improve etch uniformity.

2.1.1.5 Flash

Once the remainder of the substrate has been removed, the devices are placed into a hydrofluoric acid bath to remove the remainder of the stop-etch layer, which finally yields a high optical quality planar surface. The problem with using hydrofluoric acid is that it attacks glass. Therefore the glass slides that the devices are mounted on must be protected

Currently the slides are encapsulated in black wax. The only way to remove the wax once the flash has been achieved is to use toluene. Unfortunately this leaves a residue on the

surface of the device that is difficult to remove. Thus the optical quality of the device suffers. Not to mention the problems the residue may be causing with the contacts. Therefore an extra cleaning step has been implemented and is discussed below.

A new method of protection has been investigated. Gel-Pak Inc. sells a gel film that adheres to glass and glasslike materials but can be removed without the use of solvents. Thus this new film removes the need for the use of the black wax and may be removed easily when the flash is completed.

Several issues still need to be resolved as to the use of the gel film. The first is that the top surface of the glass is not covered so that it is etched. Since this side is not necessary to device performance, this problem may be inconsequential. The second is that with the top surface unprotected, the acid attacks the epoxy. The result is that the epoxy peels off around the device. The device and the epoxy under the device seem to be unaffected. Two problems have been encountered when using the film. The first is that as the device is dried off after rinsing, some debris of the epoxy will deposit itself upon the device surface. This may be cleaned using methanol and a cotton swab. The second is that several devices have clouded over so that the surface becomes hazy after flashing. Because of this, the use of the Gel-Pak film has been suspended until the reason for the clouding is determined.

2.1.1.6 Post-Process Clean

In order to completely remove the black wax used in the previous section, a thorough clean is made. The clean consists of a soak first in toluene, then acetone and finally methanol. The chemicals are placed in an ultrasonic bath to further enhance the cleaning process. After the soak in methanol, the device is rinsed in distilled water and blown dry. This step has helped to obtain higher optical and electrical quality devices. Figure 9 shows the cleaning setup and figure 10 shows a device after it has been cleaned.

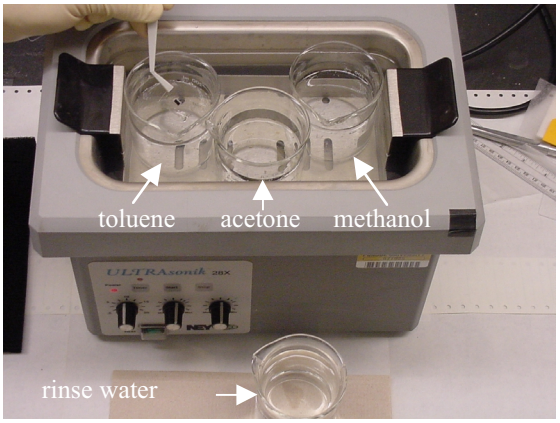

Figure 9. Cleaning setup.

Figure 10. Device after it has been cleaned. The debris on the surface is due to dust that immediately bonds to the surface after cleaning.

2.1.1.7 Contacts

The final step in fabrication is that of placing contacts upon the devices. Only one real change has been made. A cleaner, higher vacuum evaporator is being used over an older model. Figure 11 shows the differential transmission, or the change in the transmission of a device when an electric field is applied, for a device contacted with the old evaporator. The data should be symmetric with respect to the applied field. In other words the data from a positive applied field should lie on top of the data of a negative applied field, which is not the case in figure 11. Figure 12, however, shows the differential transmission of a device that had its contacts applied with the new system. The data shows the contacts to be more symmetric than in figure 11.

There are still other ways in which to improve the contacts [2]. First of all, evaporated gold does not make a good ohmic contact to GaAs [3]. The deposited gold is more of a Schottky barrier than an ohmic contact [4]. A potential improvement to this problem is to anneal the contacts. This is usually done by heating the material to several hundred degrees anywhere from several seconds to several minutes depending on the materials used [5]. This allows the gold to diffuse into the material. Unfortunately the MQW devices are too thin to heat. Other methods such as laser annealing may be possible but need to be further investigated [6]. The electrical engineering department also has an electron-beam evaporator that may yield better results than thermal annealing [7]. Other metals such as aluminum or alloys such as gold-germanium (AuGe) may also be more suitable for contacting to GaAs [7-9].

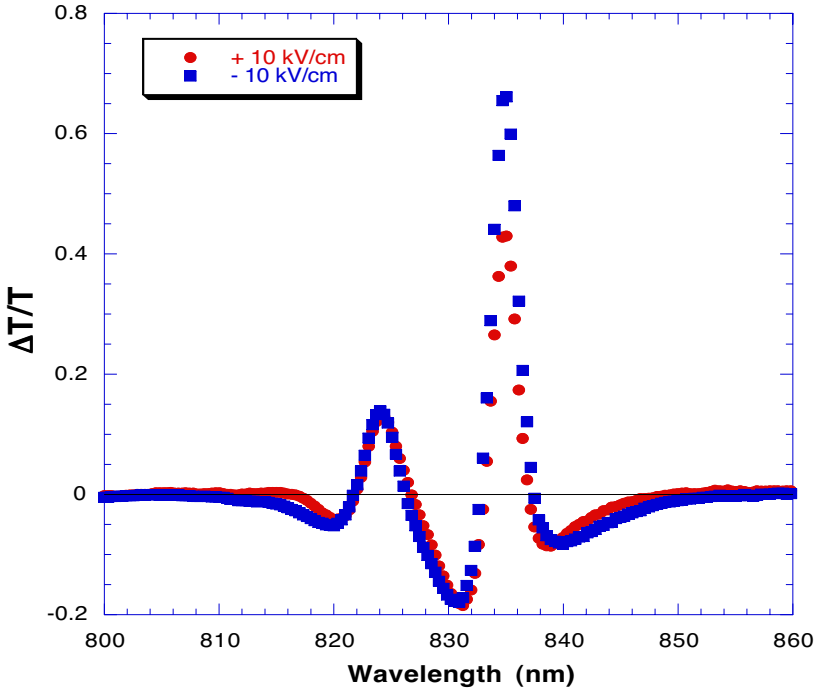

Figure 11. Differential transmission of BH13 showing field

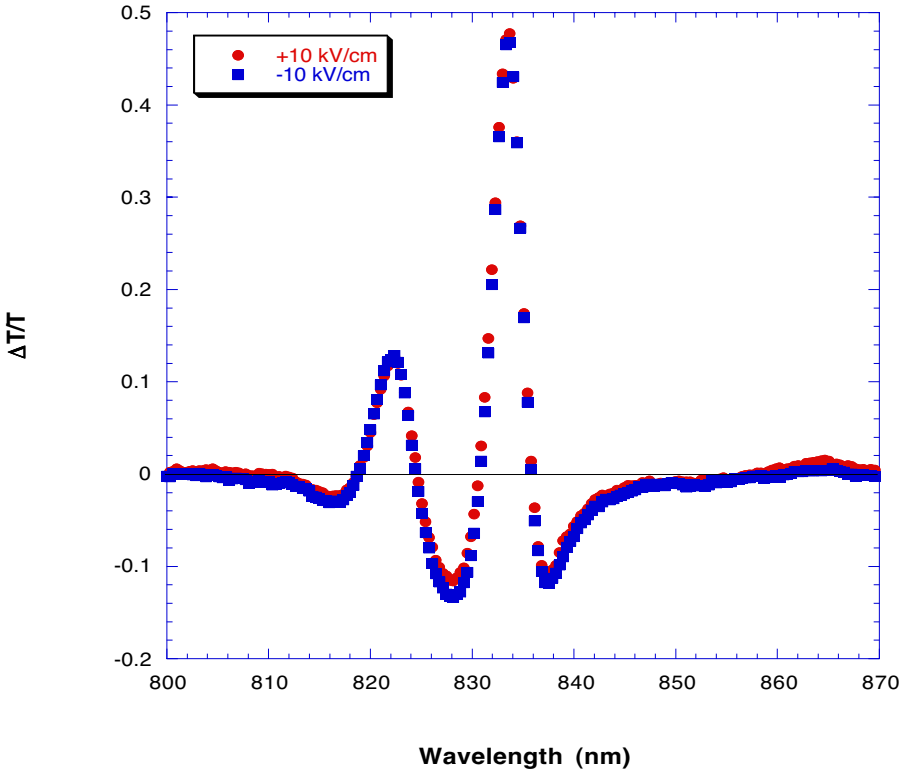

Figure 12. Differential transmission of BH39, an optimal device.

2.1.2 Experimental Set-up

An Optical Coherence Imaging (OCI) system was developed for this project to investigate the use of optical coherence imaging for imaging into the sandstone. The OCI system (Figure 13) consists of a mode-locked Ti:sapphire laser (120 femtoseconds (fs) pulses with 100 MHz repetition rate), a modified Mach Zehnder interferometer with a sample arm and a reference arm, and a photorefractive multiple quantum well (PRQW) device[Nolte, D.D., 1999] that is the dynamic holographic film. An electric field (DC 10 kV/cm) is applied in the plane of the device. This configuration is called transverse-field geometry that uses the Franz-Keldysh effect. In the interferometer, a de-magnified telescope (4:1) is used in the detecting arm that decreases the beam diameter to 1.0 mm on the sample. As a result, the intensity increases about 16 times at the sample. Two lenses with the same 150 mm focal length are separated by twice the focal length to form a 4-F system (Figure 14).

In this 4-F system, the sample is placed at the focal plane in front of the first lens and the PRQW device is placed at the focal plane in back of the second lens (Figure 14). The plane that is halfway between the lenses is called the Fourier plane or the transform plane. The 4-F system projects a 1:1 image of the sample onto the holographic film. A spatial filter is located at the Fourier plane of the 4-F system to reject part of the scattered light from the sample, and allow the ballistic components to travel to the device. The signal beam is interfered with the reference beam when the optical path lengths between the signal and reference arms are matched to within a coherence length of the laser by adjusting the translation stage in the reference arm. The interference fringes are imprinted onto the holographic film. The holograms are reconstructed using a degenerate four-wave mixing configuration. The first order diffracted signal from the reference beam is imaged onto the surface of a cooled CCD camera (RTE/CCD 1317, Princeton Instruments) with a 150 mm focal length lens, while an aperture is used to cut off zero order beam. The efficiency of the four-wave mixing is optimized by adjusting the wavelength and bandwidth of the laser, the size and position of the aperture, and the relative intensities between the signal and reference beams.

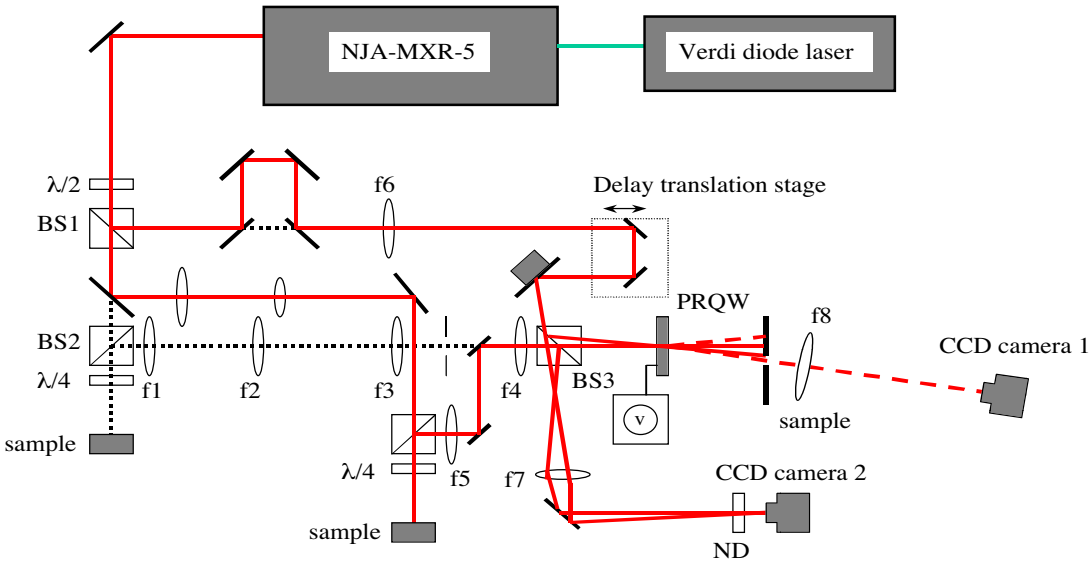

BS1, BS2: polarization beam splitter. BS3: 50/50 beam splitter.
f1=200mm, f2=100mm, f3=150mm, f4=f5=150mm, f6=500mm, f7=50mm, f8=150mm.
ND: Neutral Density Filter

Figure 13. The design and modifications of optical coherence imaging. The red lines represent the modified setup and the dash lines are from original setup.

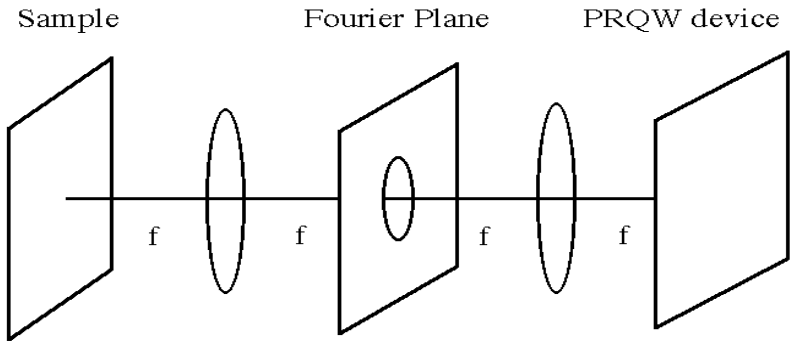

Figure 14. Two lenses form a 4-F configuration to get 1:1 imaging between the sample and PRQW device.

2.2 MICRO-MODEL

2.2.1 Sample Preparation

This section gives a description of the procedures for performing optical lithography; complete details are given in the manufacturer's manual (Shipley, 1982) and by Thompson, Willson and Bowden (1994).

In optical lithography a pattern is transferred using a visible light image to a photo-sensitive polymer layer called photoresist. This layer acts essentially as photographic film. When a region of the photoresist is exposed to a sufficiently large integrated intensity of blue light, a photochemical reaction within the photoresist makes the region soluble in a special developer solution (usually just a base). The unexposed photoresist is not soluble, so after development the photoresist layer contains a negative image of the original light pattern. In all of our work we have used Shipley photoresist types 1805 and 1827, and their standard developer (Shipley, 1982). The image has been transferred to the photoresist in two different ways. In one method (Figure 15, left) a photomask is put in direct contact with the photoresist and the exposing light is transmitted through the mask. This mask is typically an opaque metal layer on a glass substrate, or a small portion of an ordinary video transparency sheet onto which the appropriate pattern has been printed. With this contact configuration the mask pattern is transferred in a 1:1 fashion to the photoresist sample; i.e., without magnification or reduction in size. We use this method for making the coarse (i.e., largest scale) features of the micro-models. The smallest sample features are made by projecting the mask pattern onto the photoresist through a microscope objective. We employ a specially modified optical microscope which enables the image of the mask to be focused onto the sample at the same time as the sample is in focus to the observer. Projecting through a 50x objective yields a 50:1 reduction in the size of the image relative to the scale of the mask. In this way we can routinely achieve sub-micron feature sizes at the sample.

Construction of a complete micro-model involves several steps (Figure 16). The first is to transfer the pattern of the desired flow geometry into a photoresist layer – this is accomplished using optical lithography as just described. The resulting glass substrate/photoresist layer will form the bottom and sidewalls of the final micro-model. The top wall (ceiling) of the micro-model is formed by a second glass coverslip. This "top plate"

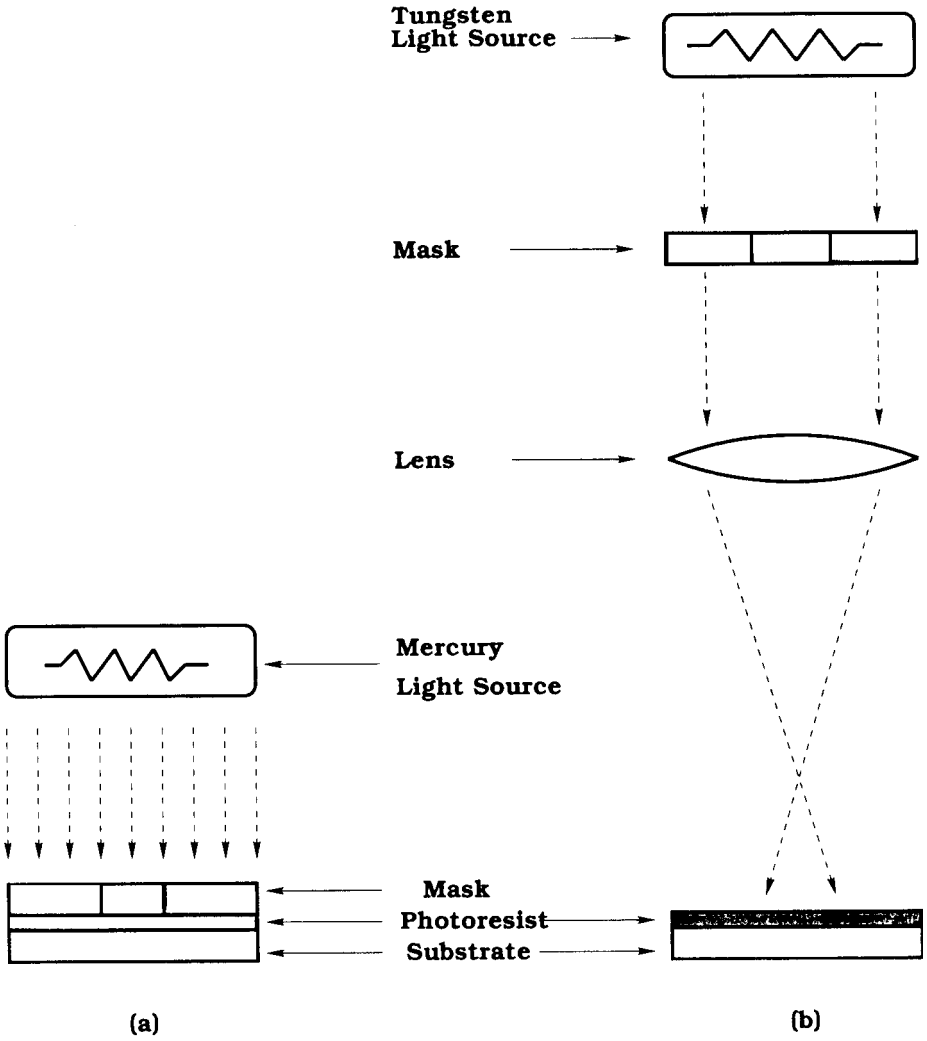

Figure 15. Schematics of the procedures used for optical lithography. Left: contact lithography. Right: projection lithography.

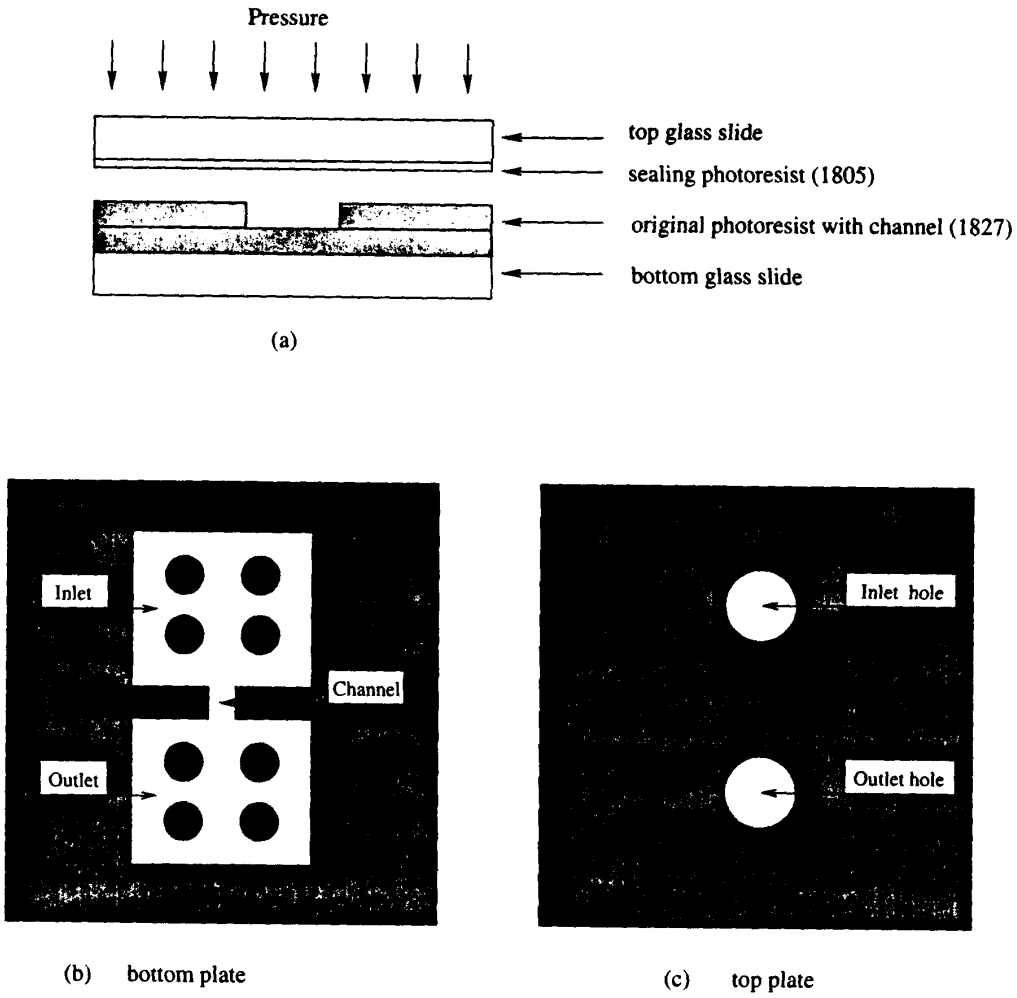

Figure 16. Micro-model layout. (a) Side view showing bottom plate containing micro-model pattern and top plate just prior to bonding. The glass slides are cover glasses 200 microns thick. The photoresist layers are 0.5 micron (type 1805 photoresist) and 2.7 microns (type 1827 photoresist). (b) Arrangement of inlet, outlet, and sample (channel) regions. (c) Inlet and outlet holes are drilled in the top plate.

is bonded to the bottom layer using another layer of photoresist – this bonding is accomplished by bringing the two glass coverslips into contact with gentle pressure (approximately 1 atm, applied in a special holder in which a flexible plastic sheet is pulled against the sample by an applied vacuum) immediately after application of photoresist to the top plate (Figure 16a). The top plate also contains two holes (approximately 1 mm in diameter, drilled ahead of time) that serve as inlet and outlet for the finished micro-model (Figure 16c). The inlet and outlet regions are fairly open spaces (approximately 4 mm on a

side) on the micro-model, and contain "pillars" which are approximately 0.5 mm in diameter to prevent collapse of the structure (Figure 16b). The working region of the micro-model is the area labeled as "channel" in Figure 16b. This is where a percolative pattern is created in the bottom photoresist layer.

2.2.2 Flow Measurement Apparatus

A schematic of the flow measurement apparatus for the micro-models is shown in Figure 17. This apparatus is used for simultaneous measurements of flow rate and optical characterization of the geometries of the various phases within the sample. This apparatus contains (1) two pressure sensors to monitor the input and output pressures, and (2) a video camera interfaced to an optical microscope to image the two-phase displacements experiments.

To perform a flow measurement on a micro-model, the micro-model is initially saturated with a fluid such as silicone oil, which is inserted through the "outlet" region in Figure 17. A second fluid, such as nitrogen gas, is then introduced through the inlet region. The flow rate of this second phase is measured using video microscopy together with an "on-chip" flow capillary. This capillary is a long narrow flow channel that is arranged to be in series with the sample and is located between the sample and the outlet region, as shown in Figure 18. The meniscus of the second fluid is tracked via microscopy as it moves along the measurement capillary, and the flow rate calculated from the known dimensions of the capillary (typically 0.2 mm wide and 2.7 microns deep). This method makes it possible to measure extremely small flow rates very quickly. All measurements are conducted at room temperature (temperature stability better than 0.5 degree Celsius during a measurement), with the apparatus located within one of the clean bench environments.

The measurement of *IAV* is also accomplished with our video microscopy setup. For this we capture the image of the micro-model and do image processing with the computer interfaced to the camera. The captured image is processed using thresholding techniques to determine the areas occupied by both fluids and the interfacial area, both of which are crucial for our studies.

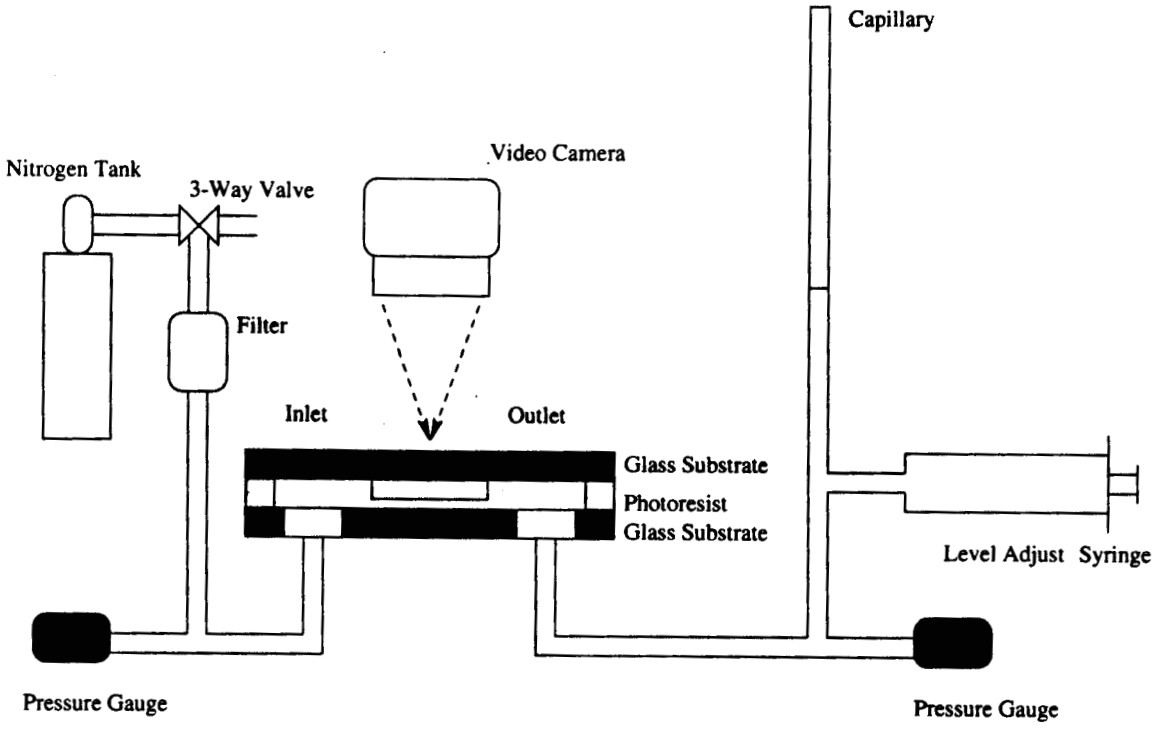

Figure 17: Apparatus used for measurement of flow rates and imaging of fluid geometry within a micro-model. The pressure sensors are piezoelectric sensors (model PX550C1 from Omega Engineering). The video camera system is a SPOT-1 RT color system (Diagnostic Instruments, Inc.) interfaced to a Macintosh G4 computer.

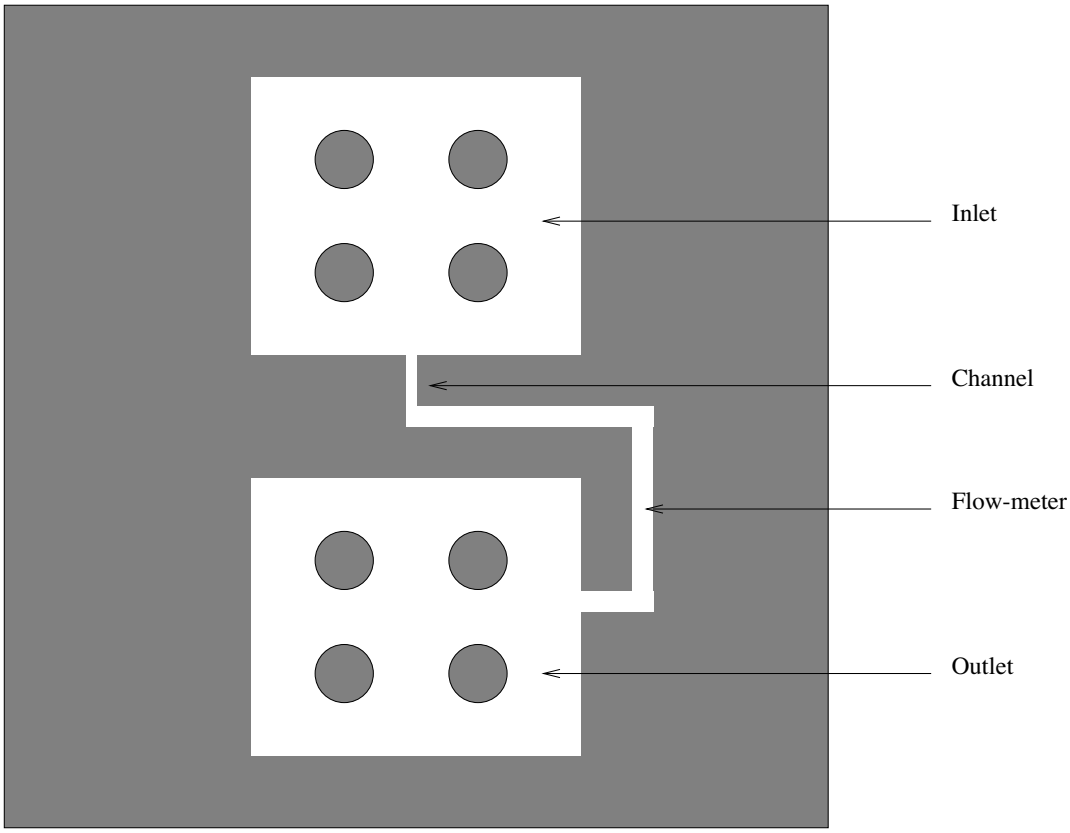

Figure 18. Micro-model with an "on-chip" capillary for the measurement of flow rates. The percolative flow structure is located in the region labeled “channel.”

2.3 Wood’s Metal Injection

2.3.1 Sample Preparation Procedure

2.3.1.1 Sample Preparation for Injection

For the measurement of absolute flow rate and for the Wood’s metal injection experiments, whole core samples from blocks of sandstone are used. The samples are cored to a diameter of 52 mm and have a length of 94 mm. The samples are coated with epoxy. The purpose of the epoxy is two-fold. First, the epoxy is used to increase the diameter of the

sample by 52 mm to provide a competent sealing surface. The second purpose of the epoxy coat is to seal the surface pores of the sample to prevent dominant flow paths forming along the surface of the sample. The procedure for applying the epoxy coats includes: (a) applying a thin layer of epoxy to the surface the sample and letting the thin coat of epoxy harden; (b) placing the thinly coated sample in the center of a tube with a diameter of 104 mm; and (c) filling the remaining space in the tube with more epoxy and letting the epoxy harden. Measurement of the sample porosity is made prior to and after coating with epoxy using a wet/dry method.

2.3.1.2 Sample Preparation for IAV Measurements

After the sample has been injected and post-injection flow measurements have been made, the sample is sampled destructively to obtain information on porosity, saturation of the sample with Wood's metal, and interfacial area per volume (IAV). The Wood's metal injected sandstone core is flushed with isopropyl alcohol to remove any remnant ethylene gylcol in the sample. The flushed sample is heated in the oven at a temperature of 54 ^{o}C for several days to evaporate the any remnant isopropyl alcohol. Then, the central portion of the sample is used for the investigation of IAV. The sample is cut to a 25.4 mm by 25.4 mm by 100 mm rectangular prism, and then sectioned into 4 pieces measuring approximately 25.4 mm by 25.4 mm by 25.4 mm. The size of the sample is controlled by the sample holder of the Scanning Electron Microscope (SEM). After cutting of the sample to the required size, the surfaces (perpendicular to the global flow direction during injection) of the four sections are polished on a polishing wheel (15 micron powder size) to create a flat polished surface.

2.3.2 SEM Scanning Procedure for Sandstone Samples

Using a Scanning Electron Microscope enables the collection very high magnification images of the pore space and metal-filled pore space in the sandstone samples. The SEM used for this project is a JEOL 35CF operated with an accelerating voltage 25kv, an objective

aperture setting of #2, a working distance of 39 mm and a condesner lens current of 2.00 to 3.00.

To ignore topographic information from the SEM images, the SEM is operated in a point by point scanning mode using the backscattered (Backscatter Electron Image - BEI) and COMP mode settings. A slow scanning speed is used because the signal is weak and noisy. Digital images are collected with IMIX software installed in a computer, which is connected to the SEM.

The contrast in the resulting image is determined by the material type (atomic number) on the sample surface (Wood's metal, sandstone, air). In the initial testing, the sample was injected with epoxy after being injected with Wood's metal. The epoxy-filled portions of the pore space represented the location of the ethylene gylcol. For samples with a high saturation of Wood's metal, it became difficult to inject epoxy into the sample. The epoxy injection step of the procedure has been eliminated. This requires us to assume that any portion of the pore space not filled with Wood's metal would be filled by a wetting phase. is:

2.3.3 Wood's metal Injection Procedure

Wood's metal injection experiments were performed on several sandstone samples. The following procedure was used for Wood's metal injection experiments:

1. Place Wood's metal tank (Figure 19). Mount the sample in holder and install sample in the other tank and seal. Fill the holding tank with paraffin oil. Close valves 1, 2, 3, 4, and 5. Place flexible heaters on the outlet tubing leading to sample and the chamber on the tubing. Monitor the temperature and pressure of the whole system.
2. Increase the temperature of the paraffin oil to 90 ^{o}C. Once a temperature of 90 ^{o}C has been achieved, maintain the temperature four hours before Wood's metal injection.

3. Apply 137.9 kPa gas pressure to Wood's metal tank. Open valves 1 and 4. Open valve 2 to let melted metal flow into sample tank until the sample is completely covered by metal as indicated by the level detector.
4. Close valves 1 and 2. Heat the outlet tubing and chamber to around 90 ºC.
5. Apply desired gas pressure to sample tank. Open valves 1 and 4 for metal injection. Use scale to monitor ethylene glycol flow rate. Adjust gas pressure during the injection to maintain a constant pressure. Turn off valve 1 when steady ethylene glycol flow is reached while maintaining the pressure in sample tank. Stop heating the outlet tubing and chamber.
6. Open valve 3. Open valve 2 to let metal flow from sample tank to Wood's metal tank while the pressure in sample tank is maintained at the desired value. Let the metal flow until the sample is not in contact with the metal (based on level detector).
7. Drain paraffin oil from the holding tank and let the system to cool down.
8. Relieve gas pressure when temperature is lower than 50 ºC. Open sample tank and remove sample out for further experiments and measurements.

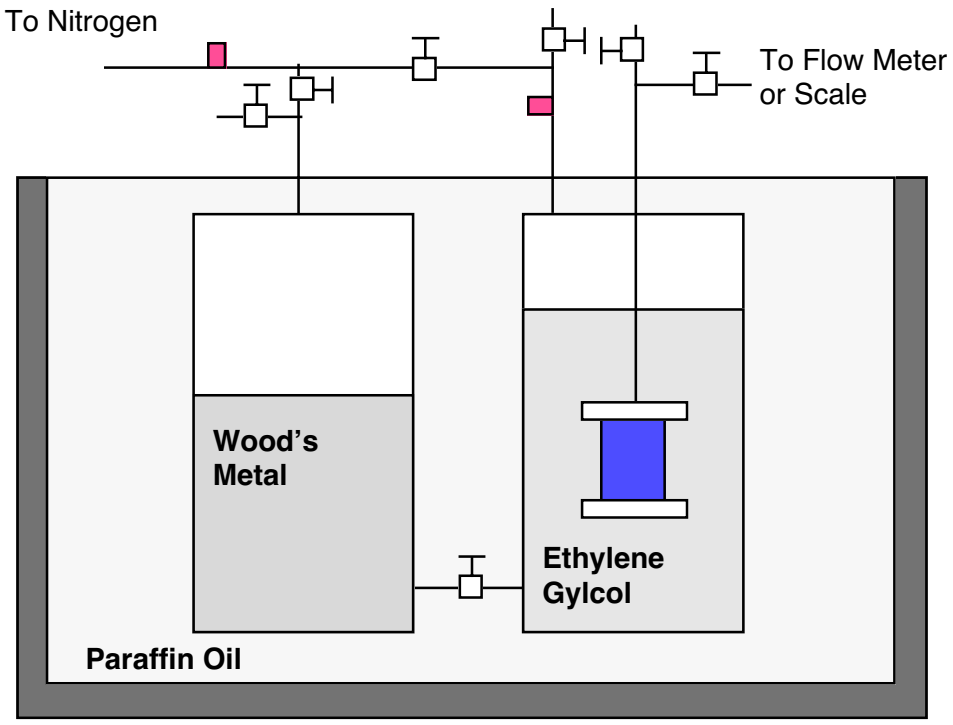

Figure 19. Schematic of Wood's metal injection system.

3.0 Results and Discussion

3.1 Optical Coherence Imaging

Optical coherence tomography (OCT) [Schmitt, 1999] is a point-by-point interferometric scanning technique in which a short optical pulse is used to interrogate dielectric reflectors along the path of pulse propagation. Each dielectric discontinuity produces an optical "echo" through coherent backscattering. The time delay of the echo is equal to twice the distance to the interface divided by the speed of light. Coherent backscatter is distinguished from incoherently scattered light through the use of a coherent reference that interfers with the coherent backscatter, but not the incoherent background. Because of this coherent/incoherent discrimination, OCT may be used to image inside strongly scattering media such as living tissue or other turbid media. OCT has enjoyed a decade of extensive progress since the first report on imaging through biological samples in 1991 [Huang et al., 1991]. For recent reviews of progress see [Schmitt, 1999; Brezinski & Fujimoto, 1999].

OCT is performed point-by-point because the coherent interference of reflected signal with the reference is detected by sweeping the reference arm through a time delay. The coherent interference produces amplitude modulation on the detected intensity that is demodulated to reject the background and extract the coherent signal. Because of the point-by-point scanning, three dimensional structures are computed tomographically. Rapid scan OCT systems have been improving, allowing nearly real-time tomographic reconstruction for interactive viewing [Tearney et al, 1997; Rollins et al, 1998].

Optics intrinsically performs parallel processing because of the free-space propagation of images. It is therefore a natural extension of OCT to consider approaches to detect entire coherent images obscured by an incoherent background without needing to scan. In such an approach it is necessary to provide a spatially coherent reference that interferes with the coherent image and to find a means of demodulating the spatial frequency.

Photorefractive holography [Nolte, 1995] is ideally suited to this task. Photorefractive materials respond (change their refractive index) to gradients in intensity rather than to the intensity itself. These materials are therefore spatial frequency demodulators. Constant illumination, as from incoherently scattered background, has no effect. On the other hand, the spatial interference fringes write holographic gratings into the

photorefractive material. The hologram diffracts a full image that may be viewed in a video monitor for each choice of reference delay. By sweeping the reference delay, a real-time fly-through video may be produced. Full-frame readout out of the hologram is observed in real time on a video camera. This system may be considered generally as a video camera with a coherence filter. This full-frame coherent imaging was demonstrated in a photorefractive crystal for the first time by the group of Paul French at Imperial College [Hyde et al, 1995].

Photorefractive quantum well devices (PRQW) were found to best suited for this application because there is no need for Bragg matching to achieve the readout. Photorefractive quantum well devices (PRQW) are dynamic holographic film that constantly refresh at rates above 1 kHz [Balasubramanian et al., 1999; Lahiri et al., 1998]. These devices have become useful for adaptive optics applications of remote ultrasound detection [Lahiri et al., 1998; Nolte et al., 2001] and for ultrafast femtosecond pulse processing [Ding et al., 1998; Ding et al., 1999]. Most of these applications have been in the 830-850 nm spectral range, but devices that operate at a wavelength of 1.06 microns are becoming available [Iwamoto et al., 2001]. PRQW devices have been used to image through turbid media in a variant to OCT called optical coherence imaging (OCI) [Jones et al., 1996; Jones et al., 1998].

Sandstone presents unique challenges to OCI because the random structure of the sand grains and void spaces are static. These static structures all produce coherent scattered light that generates speckle at the holographic film. The speckle has a bandwidth of spatial frequencies set by the system collection optics. These speckle spatial frequencies cause the photorefrctive quantum wells to respond, which obscures the coherent light scattered by the grain interfaces of interest.

As a means of better understanding OCI of static silica interfaces in sandstones, we have investigated several artificial silica structures.

3.1.1 Coherence Filter Optimization

The PRQW film in the OCI system acts as a coherence filter in front of the video camera. In principle, the image observed at the camera is proportional to only the coherent

fraction of the light striking the film. The intensity of this image is of paramount importance to assessing the performance of the OCI system, and estimating its ultimate sensitivity.

The hologram in the film is written by two intensities, the signal intensity I_s and the reference intensity I_r. There is, in addition, an "incoherent" intensity I_{incoh} that arises from random scattering of the signal beam. The hologram is played back by self-diffracting the reference. The diffracted intensity I_d is given by $I_d = \eta\ I_r$, where η is the diffraction efficiency. The diffraction efficiency is given by

$$\eta = A\ m^2 \tag{1}$$

where A is a function of applied field and wavelength, and m is the modulation of the writing beams

$$m = \frac{2\sqrt{I_s\ I_r}}{I_s + I_r + I_{incoh}} \tag{2}$$

The diffracted intensity is therefore

$$I_d = A\ \frac{4\ I_s\ I_r^{\,2}}{\left(I_s + I_r + I_{incoh}\right)^2} \tag{3}$$

3.1.2 Joule-Heating Constraint

Because the devices operate under high applied electric fields, and the laser intensities generate high photoconductivity, the devices experience Joule heating. The Joule heating must be kept below a safe value, or else thermal run-away occurs and the device may be destroyed. The Joule heating limit induces the constraint given by

$$I_s + I_r + I_{incoh} = I_J \tag{4}$$

where I_J is the maximum total intensity that the device can safely sustain. I_J is a constant (for a given applied field and proton dose on the PRQW).

The diffracted intensity therefore becomes simply

$$I_d = 4\,A\,\frac{I_s\,I_r^{\,2}}{I_J^{\,2}} \tag{5}$$

3.1.3 No Scattering

For no scattering $I_{incoh} = 0$, and the diffracted intensity as a function of the reference intensity I_r is

$$I_d = 4\,A\,\frac{\left(I_J \pm I_r\right) I_r^{\,2}}{I_J^{\,2}} \tag{6}$$

using the substitution $I_s = I_J \pm I_r$. The diffracted intensity can be maximized against I_r by differentiating, which gives the condition $I_r = 2/3\ I_J$. This gives the optimum condition for playback under maximum Joule heating:

$$I_d = \frac{16}{27}\,A\,I_J \tag{7}$$

.

3.1.4 Hologram Recording and Playback with Scattering

With a scattering intensity $I_{incoh} = R^*I_s$, Eq. (6) becomes

$$I_d = 4 \frac{A}{1+R} \frac{\left(I_J \pm I_r\right) I_r^2}{I_J^2} \tag{8}$$

This has a maximum value for the same condition as for Eq. 6 with $I_r = 2/3\ I_J$, with I_{incoh} making up the final 1/3 of I_J. The maximum diffracted signal is now given by

$$I_d = \frac{16}{27} \frac{A}{1+R} I_J \quad . \tag{9}$$

for which the reference intensity should each be set equal to twice the signal-arm intensity ($I_s + I_{incoh}$) at the plane of the PRQW device, assuming that the device is performing at its Joule heating limit. This sets the optimal conditions for holographic imaging in the presence of background light. It is interesting to note that the signal intensity I_s plays no role in this optimization condition when R is large. However, the total diffracted image falls off inversely with scattering through the factor R in the denominator.

3.1.5 Scattering of fsec pulses from planar silica interfaces (theoretical)

One of the principal objectives of this research is to image the pore structure inside sandstone. The pores are voids between silica grains. It is therefore necessary to understand the fundamental process of scattering of fsec pulses from the gap between two silica interfaces. Because of the finite pulse duration, there is a minimum resolvable gap in the longitudinal direction. In addition, multiple reflections may be expected to produce echoes and ghost reflections that could be interpreted as real structures.

A gaussian pulse has the electric field

$$e(t) = \exp\left(\pm i\omega t\right) \exp\left[\pm \frac{\left(t \pm t_0\right)^2 2 \ln 2}{\tau^2}\right] \tag{10}$$

where τ is the FWHM and is the duration of the pulse. When this pulse is incident on a dielectric layer with thickness d, the reflected amplitude is given by

$$e_r(t) = FT^{\pm 1}\left(E(\omega)\, r(\omega)\right) \tag{11}$$

where FT^{-1} is an inverse Fourier transform, $E(\omega)$ is the Fourier transform of e(t), and r(w) is the complex reflectivity given by

$$r(\omega) = r\,\frac{\left(1 \pm e^{\pm i\delta}\right)}{\left(1 \pm r^2\, e^{\pm i\delta}\right)} \tag{12}$$

where r is the normal reflectivity and

$$\delta = \frac{4\pi}{\lambda}\, n\, d \tag{13}$$

is the complex phase that depends on frequency through the wavelength and n is the refractive index of the layer.

Fig. 20 shows the power spectrum of a 90 fsec pulse and the reflectance of a 300 micron glass plate. The free spectral range of the plate is 0.75 nm compared to the bandwidth of the pulse of 11.2 nm. This large mismatch makes it possible to neglect coherent effects among the reflections, and each interface of the glass plate can be viewed as the source of an independently reflected pulse.

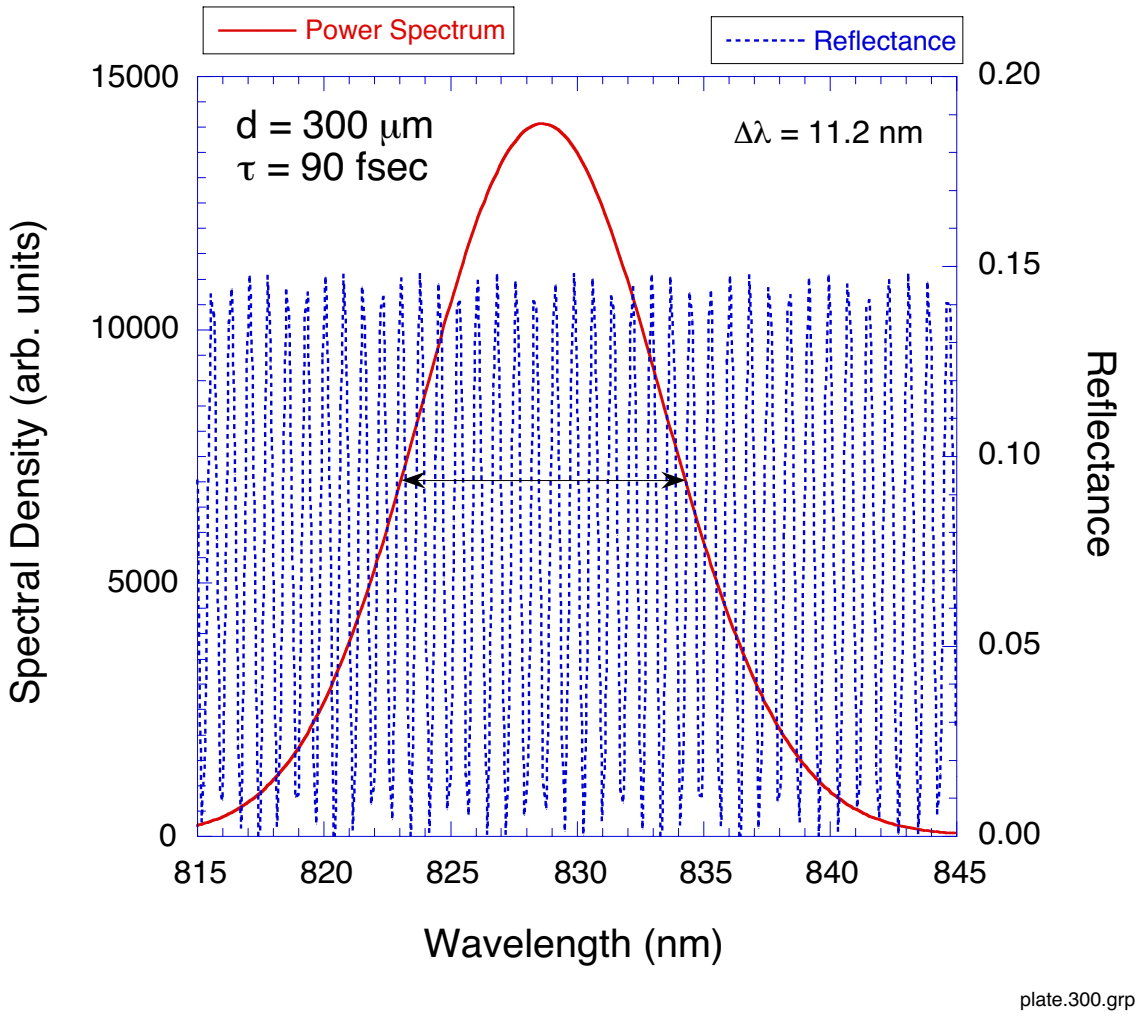

Figure 20 The power spectrum of a 90 fsec pulse and the reflectance of a 300 micron glass plate.

3.1.5.1 Spurious Echoes

The single fsec pulse will cause many reflections from the glass plate. Secondary and higher-order reflections will appear as spurious echos. If these are large, they may be mistaken for a deeper interface. Fig. 21 shows the reflected fields from a 300 micron plate. The first pulse is from the top surface, and the second pulse is from the second surface.

These reflections have nearly identical amplitudes. Analytically, the ratio of the amplitudes is given by 1-R = 96% for the glass-air interface.

The third and fourth reflections are from successive reflections within the plate. These later reflection amplitudes are considerably smaller than the primary reflections. For instance, the ratio of the third reflected intensity relative to the first is equal to $R^4 = 1.4x10^{-3}$, and each succesive reflection is reduced by the same factor. Therefore, spurious reflections will cause errors at a level of only about 0.1%. These may therefore be ignored in the experiments.

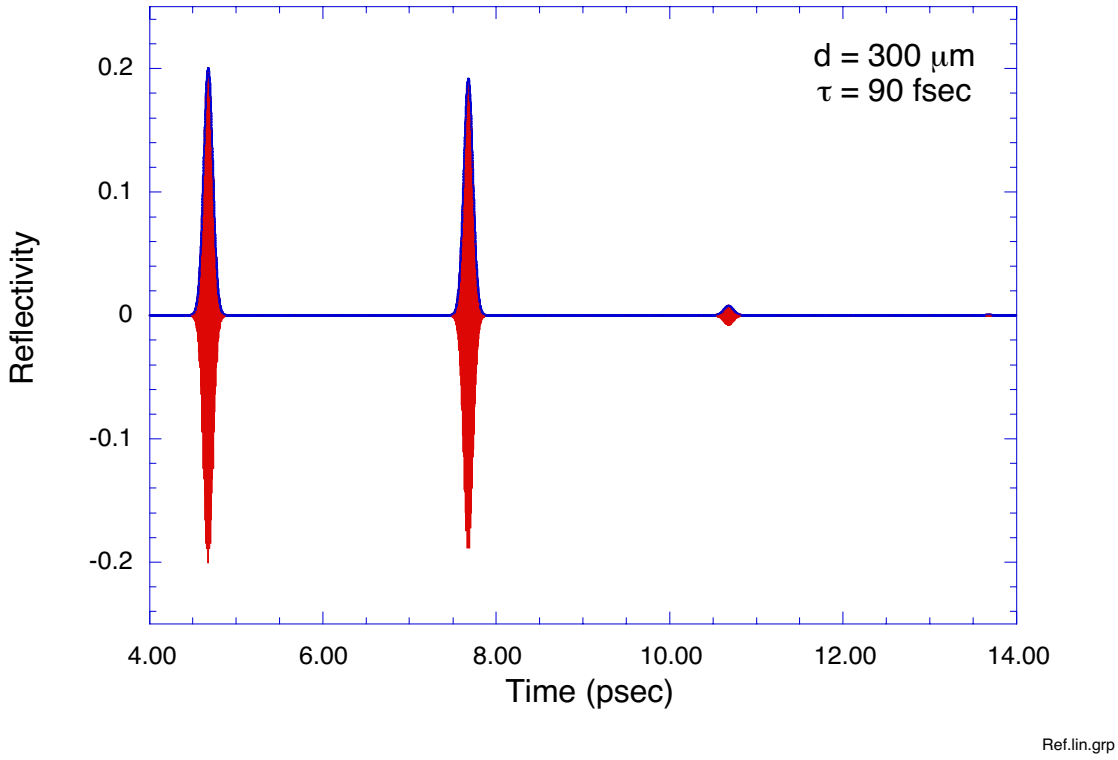

Figure 21 The reflected fields from a 300 micron plate. The first pulse is from the top surface, and the second pulse is from the second surface.

3.1.5.2 Longitudinal Spatial Resolution

3.1.5.2.1 Cross-correlation

The depth resolution of the OCI system is related to the coherence length of the probe pulse convolved with the response function of the optical system. The Rayleigh criterion for reflected pulses (based on intensity alone) to observe an air-gap (with refractive index n = 1) is set by $c\tau/4$ = 6.75 microns for a 90 fsec pulse. However, it is impossible to directly measure the temporal intensity of the pulse.

The best that can be achieved is an electric field cross-correlation of the reflected pulses with respect to an identical reference pulse. The electric field cross-correlation width is given by $\tau_x = 2\tau$. The Rayleigh criterion in this case is $c\tau_x/4 = c\tau/2$ = 13.5 microns. The cross-correlation is illustrated in Fig. 22 for a 90 fsec pulse and an air-gap between silica plates of 15 microns (slightly above the Rayleigh criterion) compared with the direct intensity profile of the reflected pulses.

3.1.5.2.2 Convolved Cross-correlation

The ideal cross-correlation shown in Fig. 22 is the limiting behavior for the holographic cross-correlation performed in this experiment. A detailed study of holographic electric-field cross-correlation in PRQW devices was performed in Ref. [Brubaker, 1994]. Because of the tilt of the reference beam relative to the signal beam (to provide a spatial frequency to the photorefractive film), the squared modulation function has a full-width of

$$\Delta x = \frac{c\,\tau}{2 \sin \theta} \qquad (14)$$

for a half-angle θ, and the modulation "walks off" from the window defined by the electrical contacts as

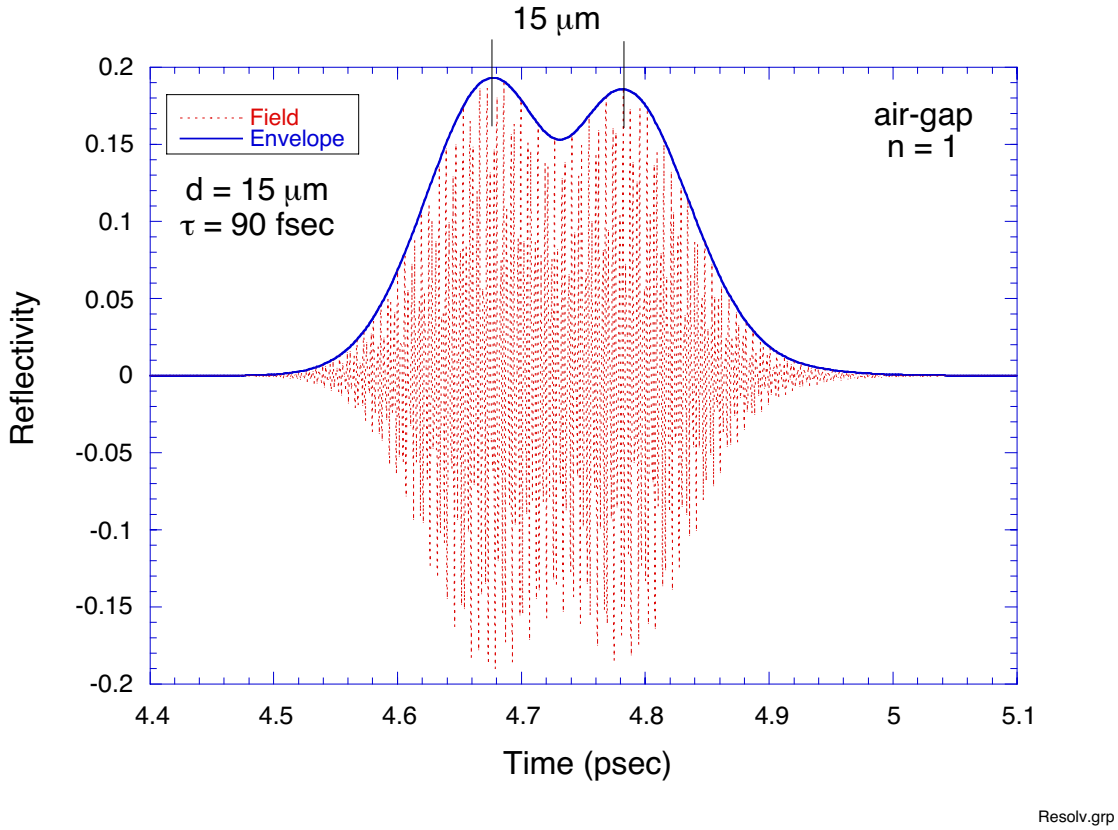

Figure 22. The cross-correlation for a 90 fsec pulse and an air-gap between silica plates of 15 microns (slightly above the Rayleigh criterion) compared with the direct intensity profile of the reflected pulses.

$$x_0(\Delta t) = \frac{c\,\Delta t}{2 \sin\theta} \tag{15}$$

where Δt is the reference delay. The ideal cross-correlation therefore must be convolved with the window function, which broadens the cross-correlation width and reduces the longitudinal resolution. It can be shown that the diffracted intensity as a function of delay Δt varies as [Brubaker, 1994]

$$I_d(\Delta t) \propto \mathrm{erf}\left\{\frac{W/2 + x_0(\Delta t)}{\Delta x\sqrt{8\ln 2}}\right\} + \mathrm{erf}\left\{\frac{W/2 \pm x_0(\Delta t)}{\Delta x\sqrt{8\ln 2}}\right\} \tag{16}$$

where W is the window width. The approximate scaling of Eq. (16) leads to a convolved cross-correlation width of

$$\tau_x^2 = 4\tau^2 + \left(\frac{2W\sin\theta}{c}\right)^2 \tag{17}$$

with a Rayleigh criterion set at

$$\Delta L_z = \frac{1}{2}\sqrt{c^2\tau^2 + W^2\sin^2\theta} \tag{18}$$

for the full-width longitudinal resolution. For a fringe spacing of 30 microns and W = 2 mm with a 90 fsec pulse, this leads to a longitudinal resolution of about 20 microns. Reducing W to 0.5 mm improves the resolution to about 14 microns, which is very close to the ideal limit of 13.5 microns. This sets the conditions under which the adaptive OCT system approaches close to its optimal performance.

It is important to keep in mind that the conditions leading to Eq. (18) rely on gaussian beams with beam waists much larger than the window width W. If either or both of the beams are focussed then the focussed beam waists take over the role of W. In fact, in the current operation of the experiments, the signal beam is focussed with a beam waist of approximately 0.5 mm, leading to a full-width cross-correlation of 28 microns, in agreement with a 14 micron Rayleigh-condition resolution.

3.1.6 Silica Interfaces

The structure of sandstone can be described as a set of multiple interfaces between silica grains or between the grains and voids. Each of these interfaces represents a dielectric

discontinuity that scatters the light. To better understand the physical process of light scattering from silica interfaces, we constructed artificial structures to interrogate with the OCI system. The first set of structures are stacks of of thin glass plates. We operated in a z-scan mode in which we replaced the CCD camera with a simple photodiode, and used a lock-in amplifier to measure the coherent reflected light. We also investigates a wedge with a linearly varying spacing between the two adjacent faces of the glass plates. We also performed OCI holographic imaging on silica spheroidal beads.

3.1.6.1 Glass Plates

Several glass plate stack structures were fabricated with differing spacing between the glass. The spacings were 6 micron, 12 micron and 18 microns. The plate thickness is 330 microns. These structures allow us to investigate the longitudinal spatial resolution of the OCI process, as well as to investigate the relative intensities of the reflected signals from the separate interfaces.

3.1.6.1.1 Six micron

The first structure had a 6 micron air gap between the two glass plates. There were ten plates in total. The z-scan interferogram is shown in Fig. 23. The front surface is at 2 mm. The first several reflections are from the 6 micron gap between the successive plates. The gap is below the longitudinal resolution of our system, as seen in Fig. 24, which is from one of the central gaps in the structure.

3.1.6.1.2 Twelve micron

Expanding the gap to nominal 12 microns places it within of system resolution. A double peak structure is clearly seen in Fig. 25 and the close-up in Fig. 26. The gap spacing of about 47 microns is seen to be much larger than the nominal value. This is likely caused by a bowing of the plates.

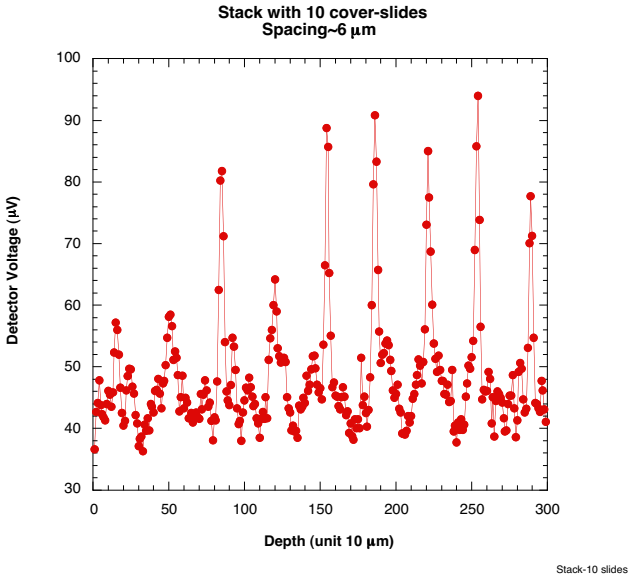

Figure 23. Scan of a 10-plate stack of glass plates with 6 micron gaps in between.

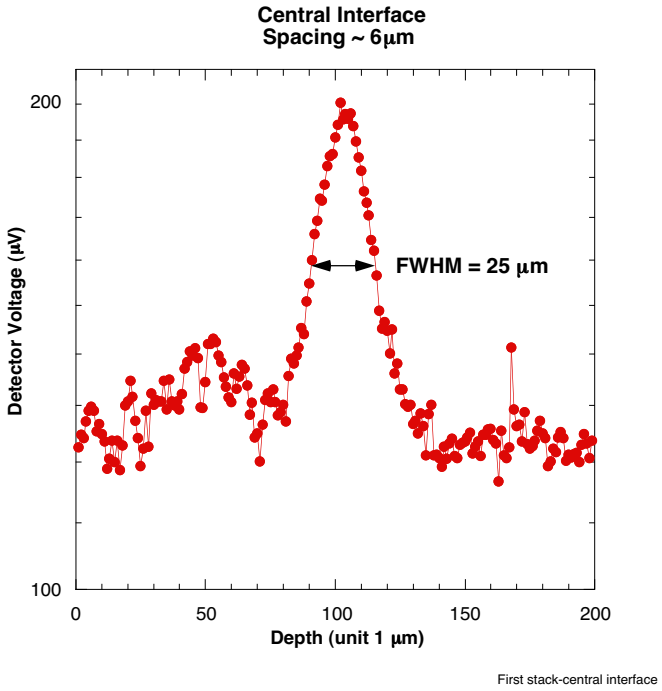

Figure 24. A close-up of the 6 micron gap between two glass plates. The gap is below the system resolution

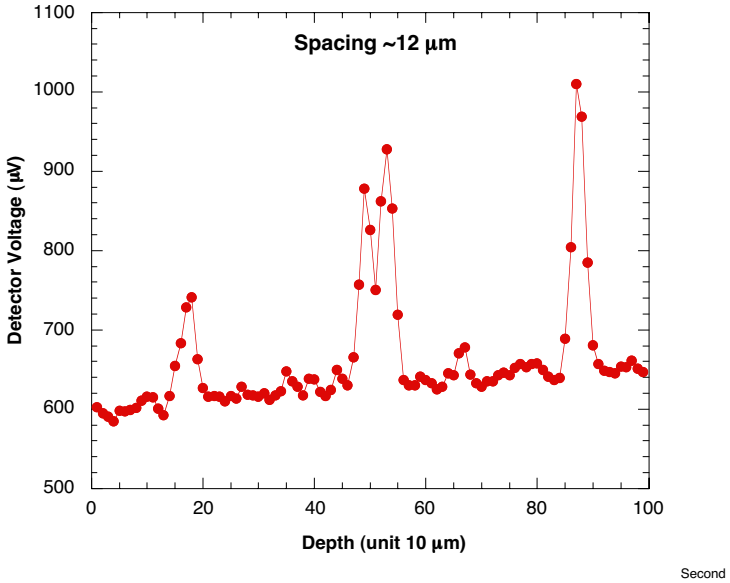

Figure 25. Scan of two plates with a nominal 12 micron air gap.

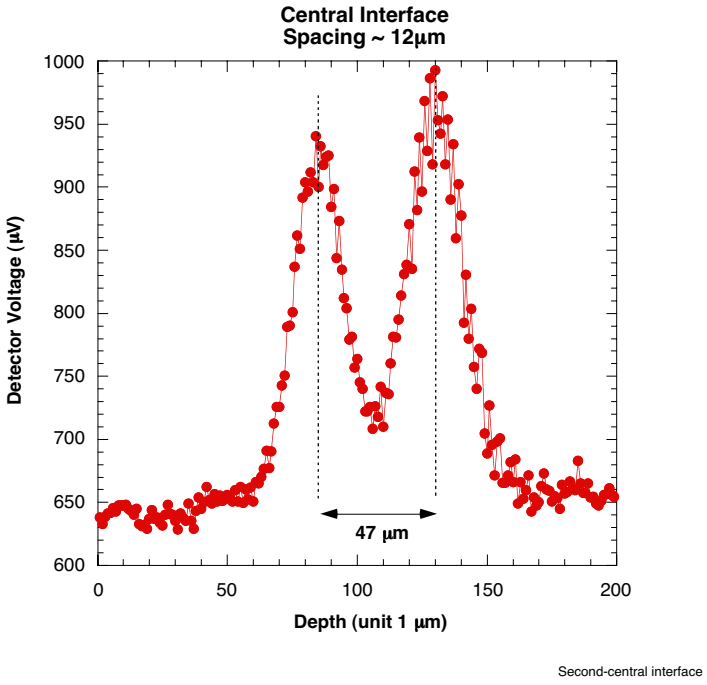

Figure 26. Close-up of the gap in Figure 22. The gap spacing of about 47 microns is seen to be much larger than the nominal value.

3.1.6.1.3 Eighteen Micron

The scans for an 18 micron nominal gap are shown in Figures 27 and 28. The gap in this case is about 55 microns.

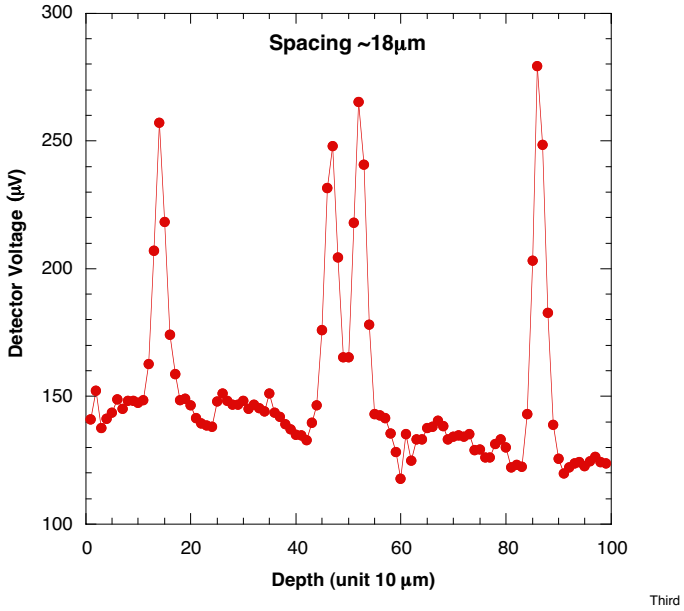

Figure 27. Scan of nominal 18 micron gap.

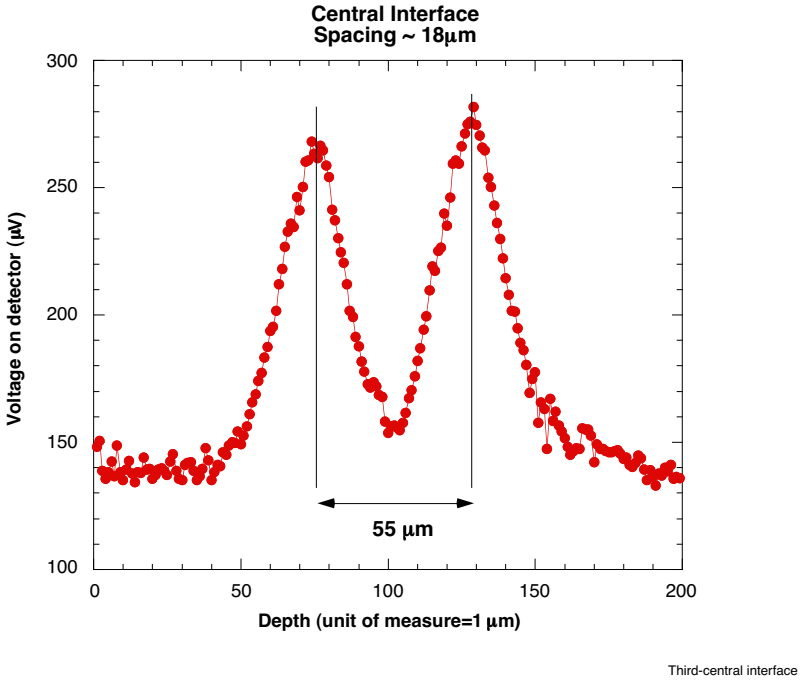

Figure 28. Central gap from Figure 24.

3.1.6.1.4 Wedge

To try to achieve a better control on the gap between the slides, we investigated a wedge structure. Scans of the wedge structure are shown in Figure 29 for successive distances from the wedge apex. The systematic increase of the peak separation is clearly seen. More tightly-positions scans are shown in Fig. 30.

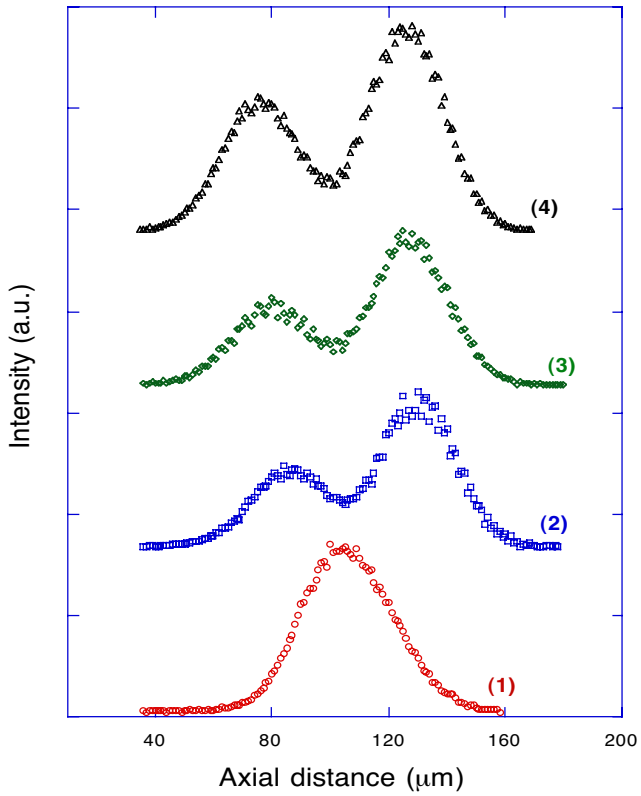

Figure 29. Scans of wedge for gaps of 40, 45, and 52 microns. The reflection peak on the right is from the upper surface of the gap.

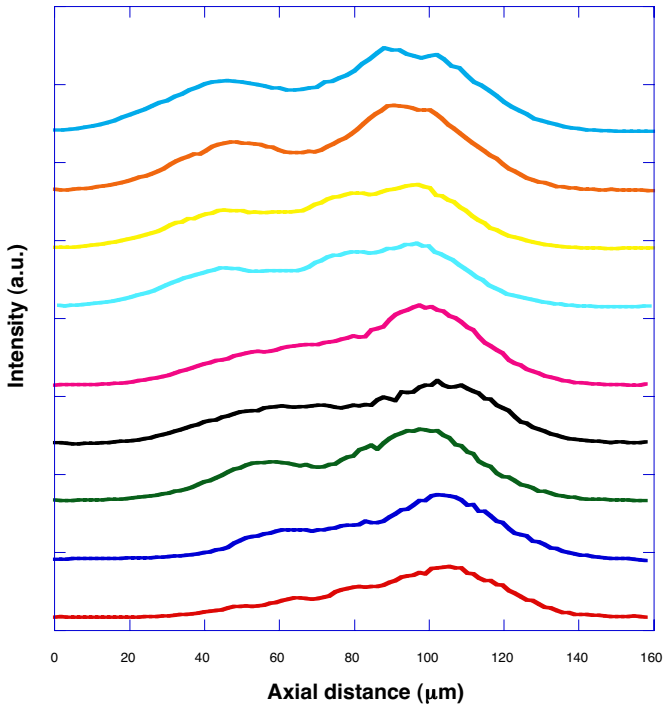

Figure 30 Scans of the wedge structure. The peak on the right is the upper interface of the gap.

3.1.6.2 Silica Beads

The planar interfaces of the artificial glass plate structures are idealized model interfaces that should mimic some of the properties of the silica grains in sandstone. An alternative model at the other extreme is the use of glass beads. These have (maximally) non-planar surfaces, and should help us understand the role of interfaces that reflect light out of the collecting angle of the collection optics. The glass beads are shown in the top row of Figure 31. The top row contains the direct image (photograph) of the beads. The middle row of images in Figure 31 contains the holographic images of the top surface of the beads. The top surface of the smooth beads was all that could be recorded in the holograms. Reflections from other positions were outside the collection angle of the optics. On the other hand, when the glass bead was placed in a drop of water, the curvature of the water droplet allowed a larger collection angle (higher numerical aperture NA) which resulted in the holographic images shown in the bottom row of Figure 31. The

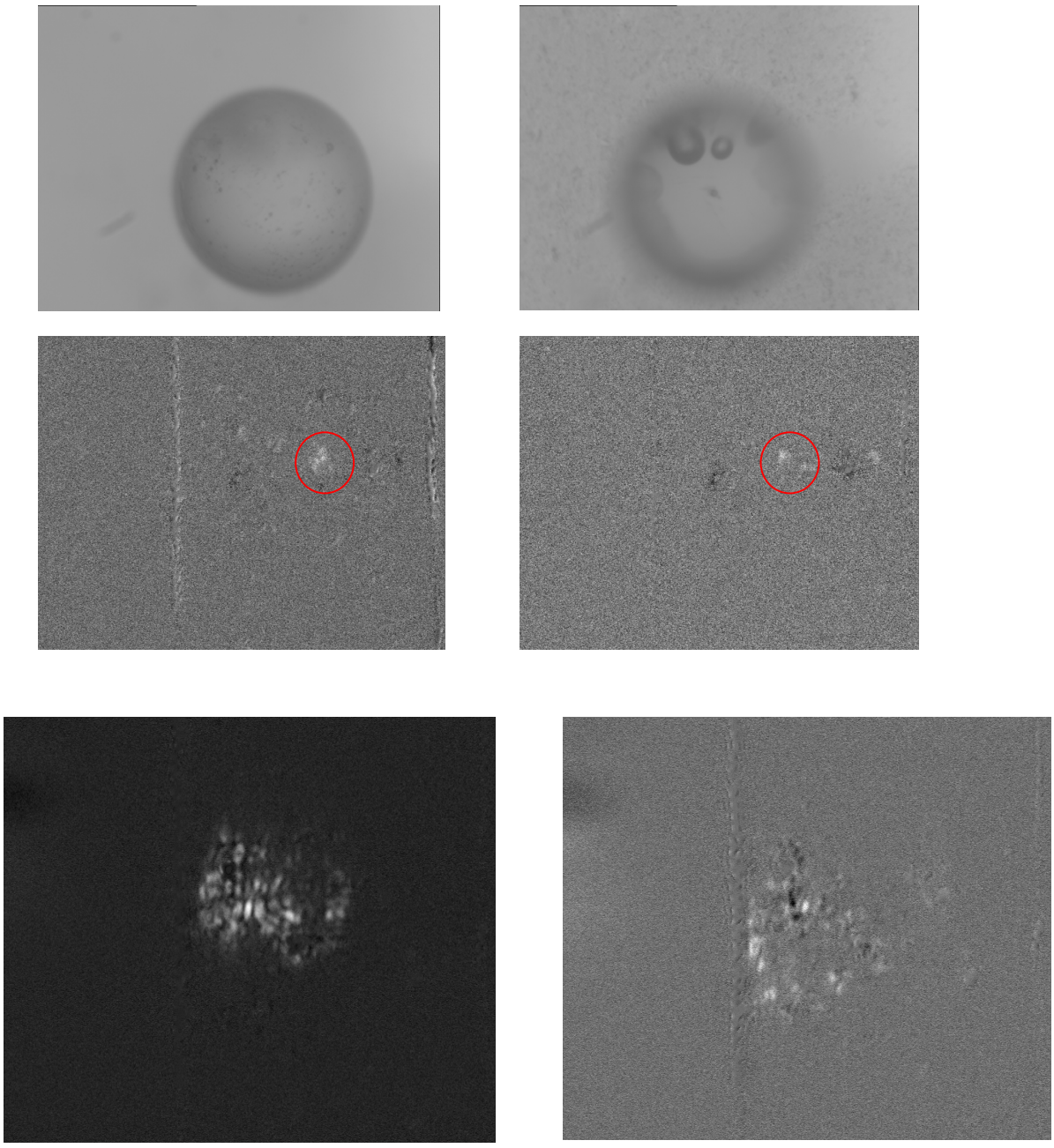

Figure 31. Top row: Direct images of two glass beads. Middle Row: Holographic images of the top surface of the glass beads. Bottom Row: Holographic images of the bottom surface of the glass beads when the beads were placed in water.

The holograms in the middle row show the top of the bead, while the bottom images show the mid-section of the bead. The difficulty of holographically imaging the bead in air, but the improved performance in water give us strong indications of the conditions under which we will obtain optimal holographic scans of the sandstone.

3.2 Micro-Models

3.2.1 IAV Results

In our work to date we have used nitrogen gas as the non-wetting fluid and either decane or silicone oil as the wetting fluid. Most of our experiments (and all of the results below) have involved decane, as it lower viscosity make it somewhat easier to work with. However, we will soon have a complete set of data for silicone oil, and a comparison with the decane results should be very instructive.

Figure 33 shows a photomicrograph of a typical sample (Figure 32) containing these two fluids. The measurements were performed by first filling the sample with decane, then forcing in nitrogen gas with a slight pressure. This pressure was then held fixed for 5 minutes (this was long enough to reach equilibrium – waiting longer produced no further changes) and a photograph was recorded. The pressure was then increased slightly and a new photograph recorded (after a 5 minute wait). This process was repeated until the sample was nearly filled with nitrogen – at that point only small trapped pockets of decane remained, and these were not removed at higher pressures. The pressure was then reduced in small steps with a photograph recorded after each step, allowing decane to reenter the sample. Eventually essentially all of the nitrogen was forced out – this completed one drainage-imbibition cycle. The data enabled us to obtain P_{cap}, S and IAV throughout the cycle. This process was then repeated, and data for additional cycles recorded. Note that during these different cycles we changed the size of the pressure increments, and also the speed with which the pressure was changed. When the two conventional variables, P_{cap} and S were plotted alone, these cycles exhibited substantial hysteresis. That is, the cycles did not repeat each other, but followed different paths.

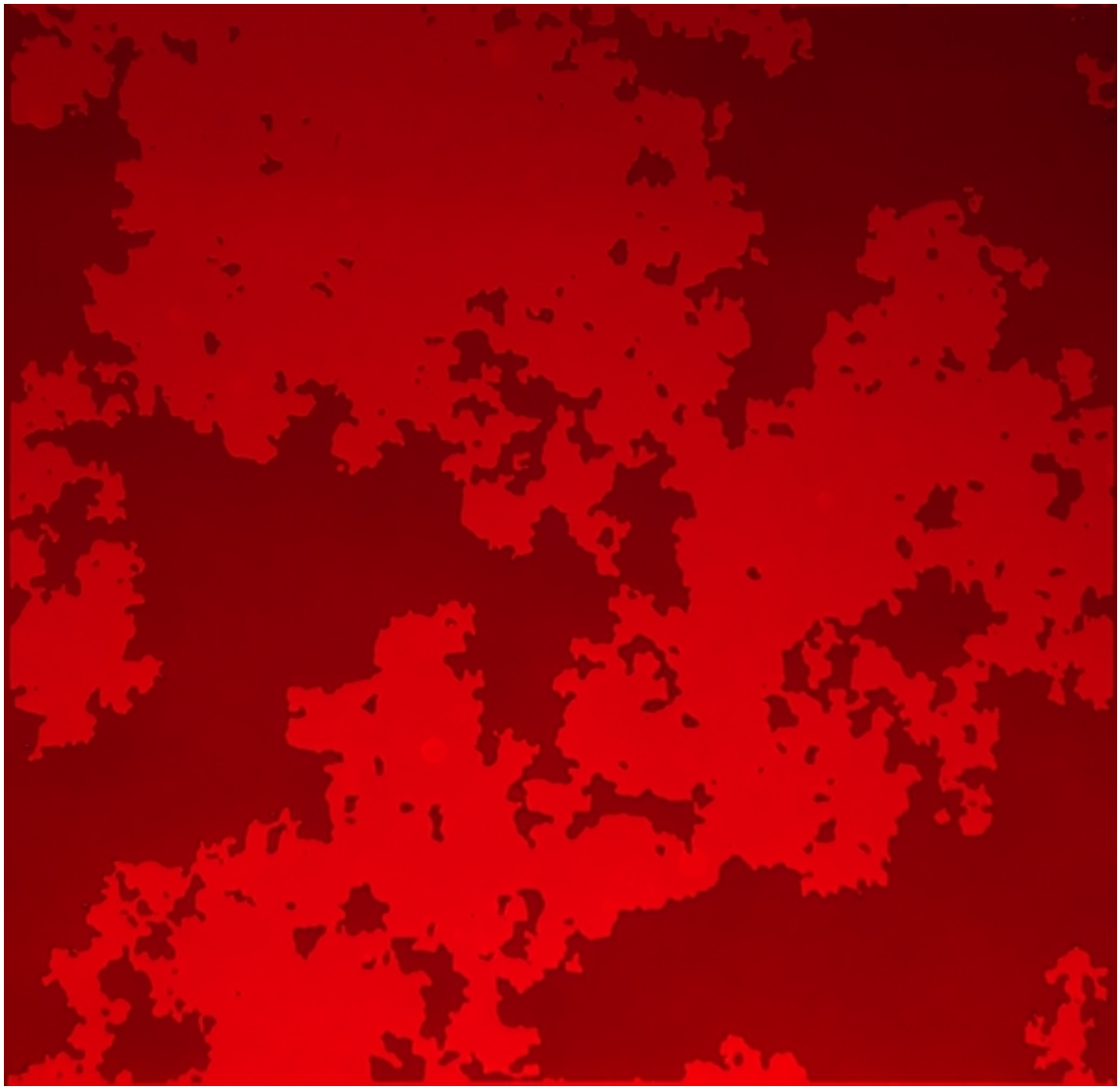

Figure 32. Micro-model showing a five tier fractal sample filled with decane. The bright areas are decane and the dark regions are inaccessible to fluid. The field of view is approximately 0.6 mm across.

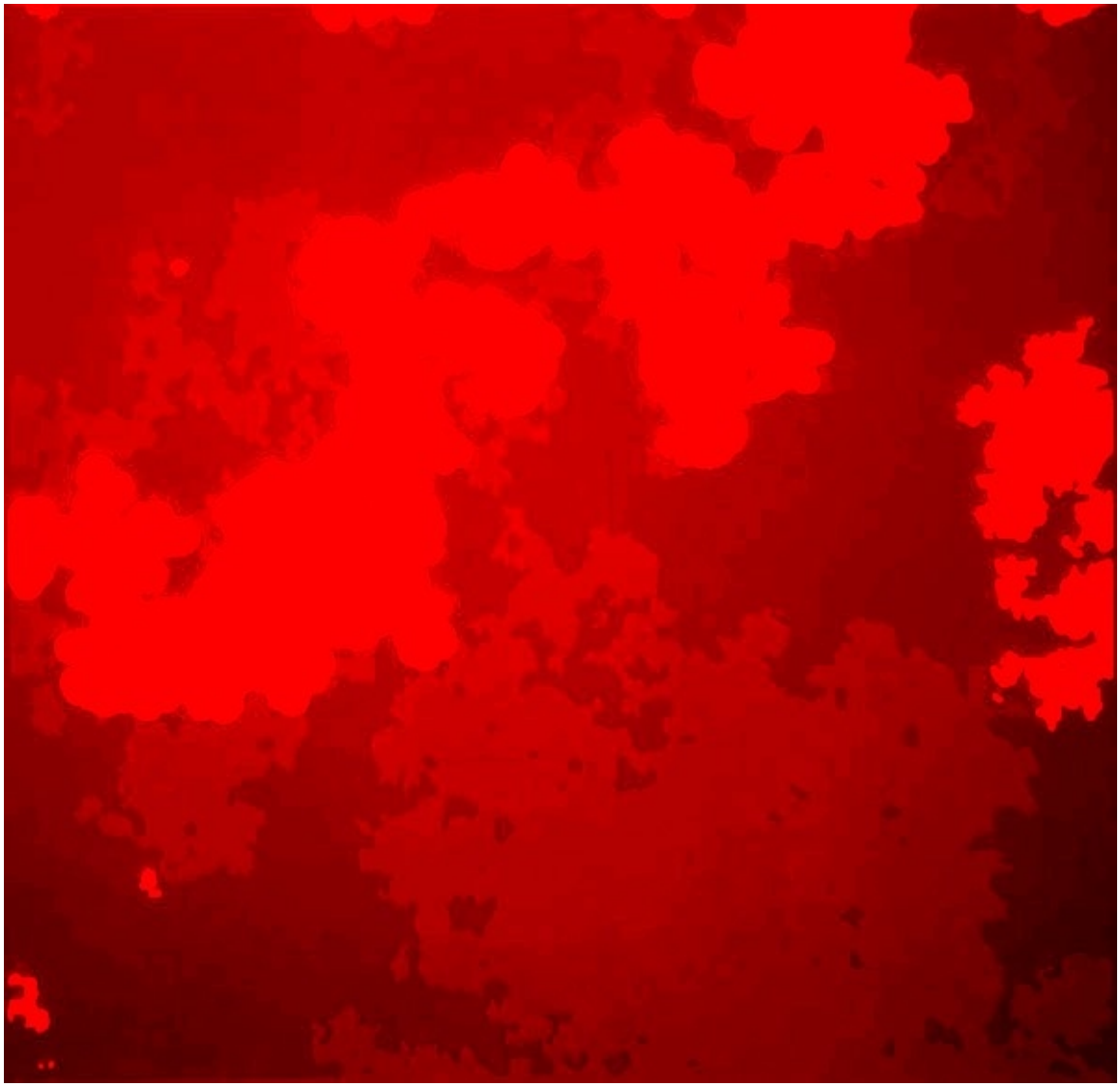

Figure 33. Micromodel from Figure 1 filled with nitrogen gas (brightest areas) and decane. The darkest regions are inaccessible to fluid.

Such hysteresis shows that the values of P_{cap} and S do not uniquely specify the state of the system. However, when the full three dimensional surface of P_{cap}, S , and IAV were considered the situation is quite different. When viewed in this three dimensional space, there is no longer any hysteresis. An example is shown in Figure 34 which gives a three dimensional plot of IAV as a function of P_{cap} and S. Note that the vertical "walls" in this plot are not regions where IAV changes abruptly; they merely indicate where the data set ends. The important point here is that the IAV- P_{cap}-S surface is single valued. This is strong experimental evidence that these three variables are sufficient to describe and characterize multiphase flow.

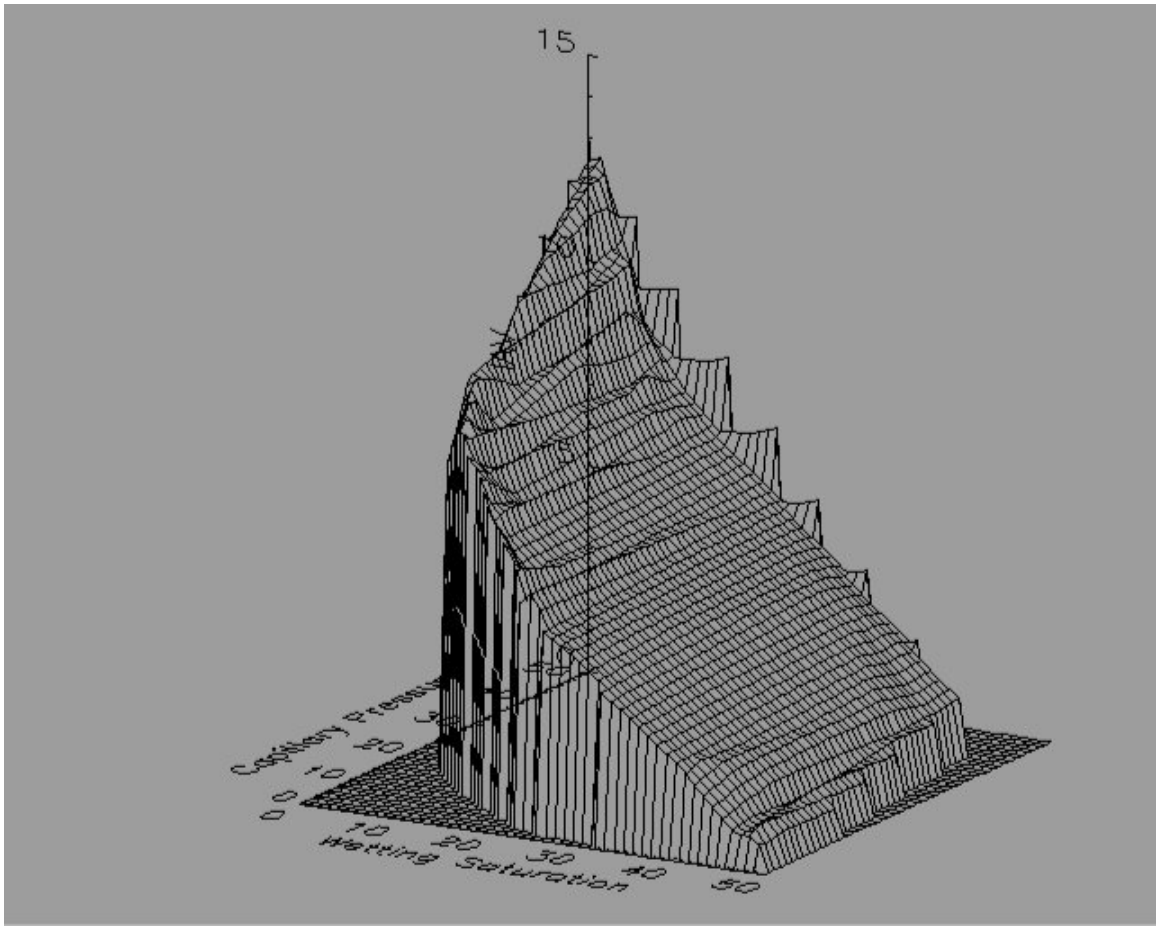

Figure 34. IAV as a function of capillary pressure and saturation for the sample shown in Figs. 32 and 33. A wetting saturation value of 50 (in the arbitrary units used here) corresponds to a sample which is completely filled with decane.

3.3 Wood's Metal Method

3.3.1 Results from Wood's Metal Injection on Interfacial Area per Volume

A goal of the Wood's metal injection experiments is to acquire interfacial area per volume (IAV) data for sandstone cores. This requires destructive sectioning (see section xx) of the core after the sample has been injected with Wood's metal. To find reliable IAV values, images of the sample are needed from which the different phases filling the pore space can be discerned.

If images from common optical microscope are used, because the brightness and contrast of the image is strongly affected by the light source and the sample surface topography, we

can hardly tell the difference among the multi-phases, the difference of the brightness can not represent different phases (Figure 35a&b).

(a) Sample image from CCD optical microscope:
5000 microns

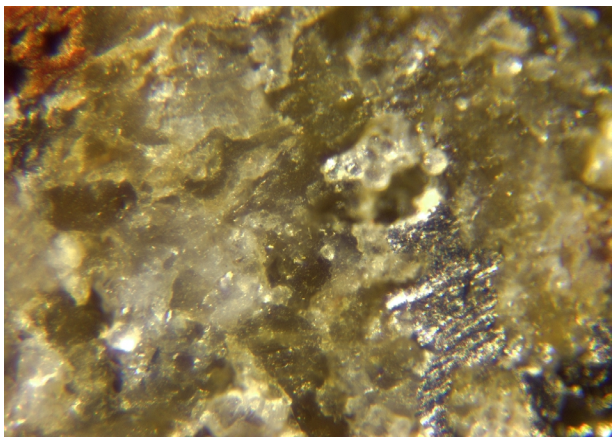

(b) Histogram of the sample CCD image:

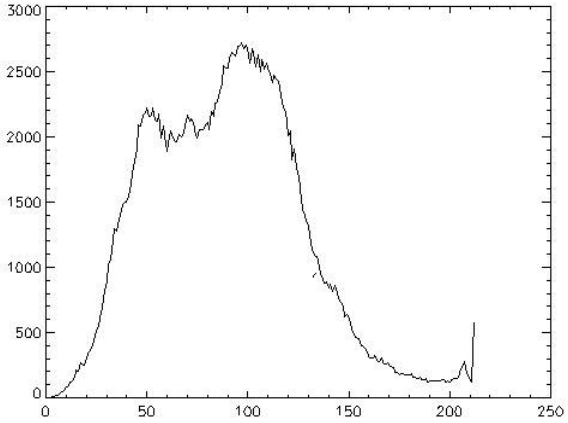

Figure 35. (a) Optical image of a surface of a sandstone sample injected with Wood's metal. (b) The histogram of intensity of the image shown in (a).

SEM images acquired in the mode described in section 2.3.1.3 enable the topography information to be removed from the image. The contrast of image is mainly determined by the material type (atomic number) on the sample surface (Figure36a). The difference shades of gray represent the sandstone (darkest shade), Wood's metal (lightest shade – almost white in the figure) and epoxy (intermediate shade). A histogram (figure 36b) of the SEM image in

Figure36b, shows three distinct peaks that represent the three distinct phases. This was not true for the CCD acquired image (Figure 35b).

a. Sample image from SEM:

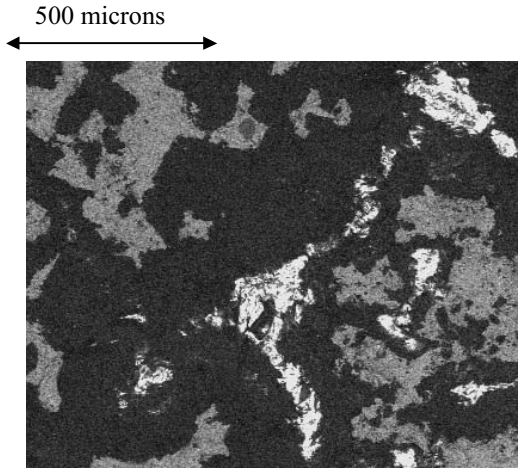

c. Histogram of the sample SEM image:

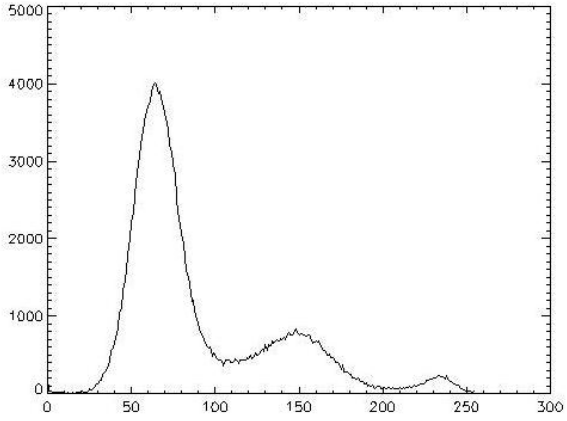

Figure 36. (a) Image of a surface of a sandstone sample injected with Wood's metal obtained using Scanning Electron Microscopy (SEM). (b) The histogram of intensity of the image shown in (a).

3.3.1.1 Image Analysis for IAV

After acquiring SEM images from the Wood's metal injected sandstone samples for several depths and locations, the images are processed to identified the various phases in the sample. A custom code was written in IDL to threshold the images for each of the phases. The number of phases is three (air-Wood's metal – sandstone, or Wood's-metal – epoxy – sandstone). First the saturation and the edge length of each phase, S1, S2, S3, L1, L2, L3 are obtained. Then based on the assumption that each phase contacts with either the second or the third phase, we can calculate L12, L13, L23, the edge length between every two phases following some simple relations:

$$L12=(L1+L2-L3)/2$$
$$L13=(L1+L3-L2)/2$$
$$L23=(L2+L3-L1)/2.$$

These relationships were tested on two simple theoretical cases shown in Figures 37 and 38. In test case 1, an image composed of a 100 pixels by 100 pixels was used with a black region of 50x100 pixels, a gray region of 50x50 pixels and a white region of 50x50 pixels. The expected results is an edge length of black phase Lb=100, an edge length of gray phase Lg=100, edge length of white phase Lw=100. If pixel overlap is considered, then Lb=100, Lg=Lw=99. The edge length between the black phase and gray phase is Lbg=50, the edge length between black phase and white phase is Lbw=50, and the edge length between white phase and gray phase is Lwg=50.

Using the IDL custom code,the image is firsted thin and then a Roberts' edge detector algorithm is used. This code found: Lb=95, Lg=93, Lw=93. Lwg=45.5, Lbw=47.5, Lbg=47.5. All edge lengths are a little bit less than expected values, but area values are identical to expected values.

Another technique developed by Berryman & Blair uses a two-point correlation function to determine the area and edge lengths. The two point correlation method found: Lb=100, Lg=99, Lw=99. Lwg=49, Lbw=50, Lbg=50. All edge lengths are closer to expected values, and area values are identical to expected values.

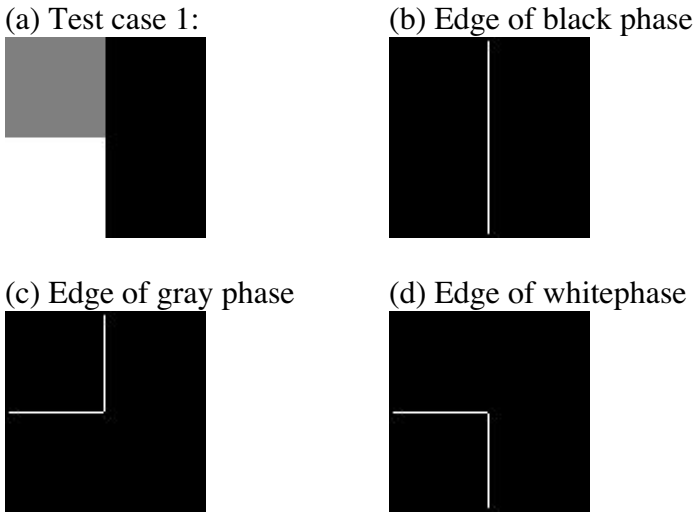

Figure 37. Test case 1 for testing the interfacial length per area algorithm.

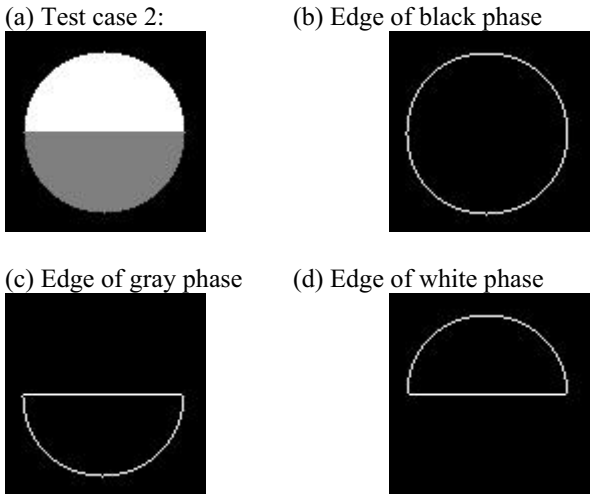

Figure 38. Test case 2 for testing the interfacial length per area algorithm.

Because pores are not square in shape, test case 2 involved determining the edge lengths and area for a bi-phase circle set in a third phase (Figure 38). The total area of the image (Figure 38) is 100x100 pixels, with 498 pixels for the black phase, 255 pixels for the gray phase, and 247 pixels for the white phase. The expected results are: Lb=251, gray phase Lg=206, and Lw=204. If pixel overlap is considered, then Lb, Lg and Lw should be less than

the values above but hard to calculate. The expected edge length between black phase and gray phase Lbg=126 or less, edge length between black phase and white phase Lbw=124 or less, edge length between white phase and gray phase Lwg=80.

Results of Roberts technique were: Lb=226, Lg=192, Lw=189. Lwg=77.5, Lbw=111.5, Lbg=114.5. All edge lengths are a little bit less than expected values, but area values are identical to expected values.

The results of two point correlation function were the same as the results of the Roberts' method. Since most edges in real images are irregular curves, both methods will lose some pixels.

Generally, the formulas we use to calculate Lwg, Lbw and Lbg from Lb, Lg and Lw are correct, and we expect some pixel loss when we try to detect edge length by digital images. To get more accurate edge length values, higher magnification is needed, however, that means more images are needed to check the same area at lower magnification and the images do not contain representative porosity.

From the image analysis, the correct saturation was calculated in both test cases but the edge lengths were only accurate to with five percent. The image analysis calculated smaller edge lengths than the actual edge length. The error in edge length calculation is caused by the limited number of pixels in a digital image and by the fact that some pixels will overlap unless they form a straight line. Since most phase edges in the real image are irregular curves, we expect a 5% system error on edge length value we will get.

The edge detection method for determining IAV was applied to SEM images of the metal-injected sandstone sample. Figure 39a shows the original SEM image from a surface in the metal-injected sandstone sample. Figure 39b, c and d show the edges for the three phase, i.e., the black phase (sandstone), the gray phase (ethlyene glycol), and the white phase (Wood's metal). Equations 3.3.1.1a-c were applied to the images to determine the interfacial length per area. The next section describes the results for sandstone sample 5 a.

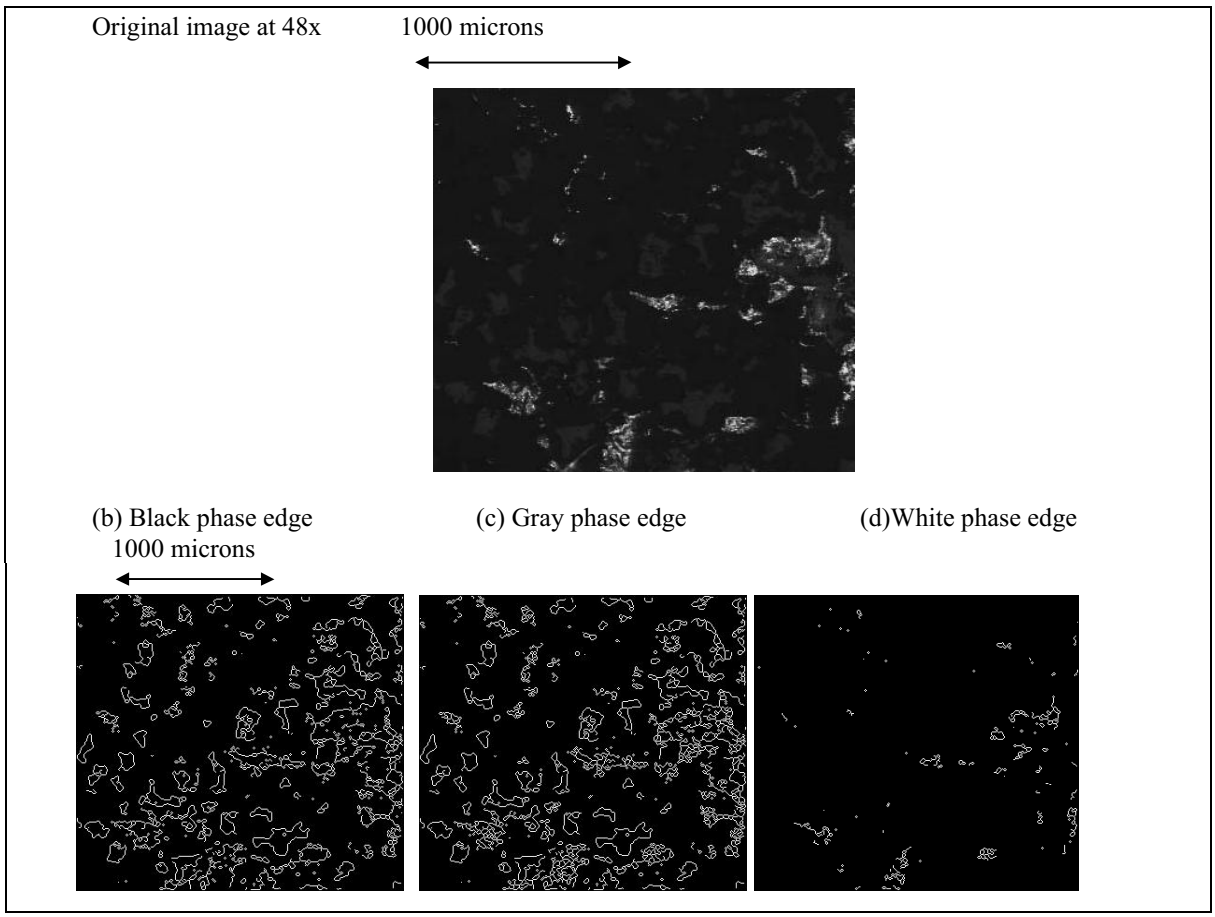

Figure 39. (a) Image of the distribution of Wood's metal, sandstone grain and empty pores obtained using Scanning Electron Microscopy (SEM). (b) Edges of the black phase – sandstone; (c) Edges of the gray phase – empty pores (or ethylene gylcol filled pores); (d) Edges of the white phase – Wood's metal.

3.3.1.2 IAV Results from Sample 5a

Unlike the micro-model experiments (see section 3.2.1), one Wood's metal experiment and the subsequent image analysis, produces one data point for the interfacial area per volume, saturation and capillary pressure curve. In the micro-model experiments, one experiment can produce 100 points of data. For the one data point, we have analyzed 80 images.

The dimensions and laboratory measured results for Sample 5 a are given in Table X1.

Table 1. Measured bulk volume and porosity for sample 5a and the injection pressure and the weight of the Wood's metal in sample 5a.	
Bulk Volume (cm^3)	191.227
Sample Porosity (%)	18.6
Injection Pressure (MPa)	0.34 MPa
Weight of Metal Injected (g)	112.59

4.0 Conclusions and Future Work

4.1 Optical Coherence Imaging

Several aspects of the processing and sample preparation procedure have been improved for the fabrication of multiple quantum well devices (MQW). These improvements have resulted in high optical quality devices. Applied fields on the devices have become consistently homogeneous using the new preparation procedure. While not a critical factor, device-processing time has also been dramatically reduced. Former processing, from cleaving the material to packaging, used to take approximately 12 hours to complete. Now a device takes less than six hours to fabricate. With the potential of using different epoxies, this time could be cut in half again. The devices fabricated are still far from perfect. There are still issues that need to be resolved and processing steps that can be improved upon.

Theoretical and experimental studies show that the optical coherence imaging system is optimized for working with sandstone. The future work for the OCI component of the project includes collecting more holographic images on sandstone and development of the fiber-optic based OCI system.

4.2 MICRO-MODELS

Ours are the first experimental measurements of P_{cap}, S and IAV in any system. The use of micro-models in this work was essential, since with most experimental systems it is not possible to obtain high quality images (required to measure IAV) of the multiple phases *in-situ* . Our central result is that the variables P_{cap}, S and IAV are sufficient to provide a complete description of multiphase flow. This result is in agreement with the general theoretical arguments of Gray and coworkers (Gray 1983, Muccino et al. 1998), and with the numerical simulations of Reeves and Celia (1991). Much work remains to be done. Our results along with the theory just cited indicates that a description of multiphase flow must include all three variables P_{cap}, S and IAV . However, this does not tell us much about the actual functional form of the P_{cap}-S-IAV relation. Theoretical means to calculate this relationship, and also compute additional quantities such as the flow rate, must still be developed. Our results will provide strong tests of these theories.

4.3 WOOD'S METAL METHOD

Analysis of the images from a sandstone sample have found that IAV values for a natural three-dimensional system (i.e., sandstone) are distributed between 50 to 210 per cm at a pressure of 0.34 MPa with an average of 110 per cm for both the rock-metal interface and the ethylene gylcol – rock interface. For the metal-ethylene gylcol interface, IAV values ranged from 0.5 to 7.5 1/cm at 0.34 MPa. We have determined that we can measure the interfacial length per area for distribution of two fluid phases through image analysis. The determination of IAV for natural sandstone samples is time-intensive. Our future work will be the measurement of IAV on sandstone for different capillary pressures and to determine the link between IAV measured on 2-D systems (micro-models) and the those measured on the 3-D systems (sandstone).

5.0 References

Balasubramanian, S., I. Lahiri, Y. Ding, M. R. Melloch, and D. D. Nolte, "Two-wave mixing dynamics and nonlinear hot-electron transport in transverse-geometry photorefractive quantum wells studied by moving gratings," Appl. Phys. B **68**, 863-9 (1999).

Brezinski, M. E. and J. G. Fujimoto, "Optical coherence tomography: High-resolution imaging in nontransparent tissue," IEEE J. Sel. Top. Quant. Electron. **5**, 1185 (1999).

Darcy, H., Determination of the laws of flow through sane, Les fontaines publiques de la ville de Dijon, Victor Dalmont, Paris, 1856, 590-594, (translated and reprinted in Physical Hydrology, edited by R. A. Freeze and W. Back, Hutchinson Ross Publishing Company, Stroudsburg, PA, 1983).

Ding, Y., D. D. Nolte, M. R. Melloch, and A. M. Weiner, "Time-domain image processing using dynamic holography," IEEE J. Sel. Top. Quant. Elect. **4**, 332-341 (1998).

Ding, Y., A. M. Weiner, M. R. Melloch, and D. D. Nolte, "Adaptive all-order dispersion compensation of ultrafast laser pulses using dynamic spectral holography," Appl. Phys. Lett. **75**, 3255 (1999).

Giordano, N., and J. T. Cheng, Microfluid mechanics: Progress and opportunities, J. Phys. Condensed Matter, **13**, R271 (2001).

Giordano, N., and J. T. Cheng, Interfacial Area, Pore Geometry and Hydraulic Properties from Micro-Models, Milestone Report (DOE Award De-AC26-99BC15207), Purdue University, March 2001.

Goossen K.W., J.E.C., T.H. Chiu, D.A.B. Miller, D.S. Chemla, Non-Alloyed Al Ohmic Contacts to GaAs for GaAs/Si Interconnect Compatibility. International Electron Devices Meeting 1989: p. 409-10.

Gray, W. G., General conservation equations for multi-phase systems: 4. Constituitive theory including phase change, Adv. Water Resources **6**, 130-140 (1983).

Grovenor, C.R.M., Au/Ge Based Ohmic Contacts to GaAs. Solid-State Electronics, 1981. **24**(8): p. 792-3.

Hassanizadeh, S. M. and W. G. Gray, General conservation equations for multi-phase systems: 1. Averaging procedure, Adv. Water Resources **2**, 131-144 (1979).

Hassanizadeh, S. M. and W. G. Gray, Mechanics and thermodynamics of multiphase flow in porous media including interphase boundaries, Water Resource Research **13**, 169-186 (1990).

Headley, William R, Processing and Characterization Methods for Transverse Field Semi-Insulating GaAs/AlGaAs Multiple Quantum Wells. 2001, Purdue University.

Huang, D., E. A. Swanson, C. P. Lin, J. S. Schuman, W. G. Stinson, W. Chang, M. R. Hee, T. Flotte, K. Gregory, C. A. Puliafto, and J. G. Fujimoto, "Optical Coherence Tomography," Science **254**, 1178 (1991).

Hyde, S. C. W., N. P. Barry, R. Jones, J. C. Dainty, P. M. W. French, M. B. Klein, and B. A. Wechsler, "Depth-resolved holographic imaging through scattering media by photorefraction," Opt. Lett. **20**, 1331 (1995).

Islam, M.S., A.H.M. Zahirul, M.Q. Huda, Advantages and Problems of Thermal Evaporation and Conventional Annealing of Metallizations for the fabrication of GaAs MESFET's. Tenth International Workshop on the Physics of Semiconductor Devices, 1999. **3975**: p. 588-93.

Iwamoto, S., H. Kageshima, T. Yuasa, M. Nishioka, T. Someya, Y. Arakawa, K. Kukutani, T. Shimura, and K. Kuroda, "Photorefractive InGaAs/GaAs multiple quantum wells in the Franz-Keldysh geometry," J. Appl. Phys. **89**, 5889 (2001).

Jones, R., S.C.W. Hyde, M. J. Lynn, N. P. Barry, J.C. Dainty, P.M.W. French, K. M. Kwolek, D. D. Nolte, and M. R. Melloch, "Holographc storage and high background imaging using photorefractive multiple quantum wells," Appl. Phys. Lett. **69**, 1837 (1996).

Jones, R., N. P. Barry, S. C. W. Hyde, P. M. W. French, K. M. Kwolek, D. D. Nolte, and M. R. Melloch, "Direct-to-Video holographic readout in quantum wells for 3-D imaging through turbid media," Opt. Lett. **23**, 103 (1998)Kim T.J., H.P.H., Ohmic Contacts to GaAs Epitaxial Layers. Critical Reviews in Solid State & Materials Sciences, 1997. **22**(3): p. 239-73.

Kittel, C., Introduction to Solid State Physics. 7th ed. 1996, New York: Wiley.

Kumar, D., Au/AuGeNi contacts to GaAs Formed by Rapid Electron-Beam Processing. Physica Status Solidi A, 1993. **139**(2): p. 433-41.

Lahiri, I., L. J. Pyrak-Nolte, D. D. Nolte, M. R. Melloch, R. A. Kruger, G. D. Bacher, and M. B. Klein, "Laser-Based Ultrasound Detection using Photorefractive Quantum Wells," Appl. Phys. Lett. **73**, 1041-43 (1998).

Muccino, J. C., Gray, W. G. and L. A. Ferrand, Toward and improved understanding of multiphase flow in porous media, Rev. Geophys. **36**, 401 (1998).

Nolte, D.D, and L. J. Pyrak-Nolte, Stratified continuum percolation: Scaling geometry of hierarchical cascades, Phys. Rev. A **44**, 6320 (1991).

Nolte, D. D. ,"Photorefractive Effects and Materials,", (Kluwer Academic Publishers, Dordrecht, 1995).

Nolte, D.D, "Semi-insulating Semiconductor Heterostructures: Optoelectronic Properties and Applications," J. Appl. Phys. **85**, 6259-6289 (1999).

Nolte, D.D., T. Cubel, L. J. Pyrak-Nolte, and M. R. Melloch, "Adaptive beam combining and interferometry using photorefractive quantum wells," J. Opt. Soc. Am. B (March) (2001).

Oraby, A.H., Characterization of Laser Annealed Au-Ge Ohmic Contacts to GaAs. Ultra Scientist of Physical Sciences, 1997. **9**(2): p. 188-92.

Piotrowska, A., Ohmic Contacts to GaAs: Fundamentals and Practice. Acta Physica Polonica A, 1993. **84**(3): p. 491-504.

Reeves, P. C. and M. A. Celia, A functional relationship between capillary pressure, saturation, and interfacial area as revealed by a pore-scale network model, Water Resource Research **32**, 2345 (1996).

Rollins, A. M., M. D. Kulkarni, S. Yazdanfar, R. Ung-arunyawee, and J. A. Izatt, "In vivo video rate optical coherence tomography," Opt. Express **3**, 219 (1998).

Schmitt, J. M., "Optical coherence tomography (OCT): A Review," IEEE J. Sel. Top. Quant. Electron. **5**, 1205 (1999).

Tearney, G. J., M. E. Brazinski, B. E. Bouma, S. A. Boppart, C. Pitris, J. F. Southern, and J. G. Fujimoto, "In Vivo endoscopic optical biopsy with optical coherence tomography," Science **276**, 2037 (1997).